ously (Morgan et al., 2000). The radial-arm water maze consisted of a circular pool measuring 1 m in diameter with six arms 19 cm wide that radiated out from an open central area, with a submerged escape platform located at the end of one of the arms. Spatial cues including a light were present on the wall of the testing room. The escape platform was placed in a different arm each day, forcing the mouse to use working memory to solve the task. On each trial, the mouse was started in one arm and allowed to swim for up to 1 min until finding the platform. The number of errors until the mouse reached the platform was recorded. After the fourth trial, the mouse was placed in a cage for 30 min and then returned to the maze and administered the fifth trial to assess memory retention. The error score was determined by the average score obtained from testing conducted during a 2 d period after training for 7 d.

Systemic lipopolysaccharide injection. Thirty-two male 24-month-old C57BL/6 mice were subjected to the systemic injection of either saline (WT, $n = 8$; TG, $n = 8$) or lipopolysaccharide (LPS) (WT, $n = 3$; TG, $n = 13$). The aged WT and TG mice were injected intraperitoneally with sterile saline or *Escherichia coli* LPS (0.33 mg/kg; serotype 055:B5; Sigma-Aldrich). In the first study, mice ($n = 3$ for each group) were killed at 4 h after saline or LPS injection and the soluble extracts of the whole brain were subjected to the immunoblot analyses using anti-IL-1β antibody to measure the total IL-1β level. The mean relative immunoreactivity of IL-β was determined using expression of actin as an internal control. In a subsequent study, the immunofluorescence intensity of IL-1β/cell ($n = 3$ for each group), the immunofluorescence intensity of 8-oxo-dG/mitochondria ($n = 2$ for each group), and the magnitude of the long-term potentiation (LTP) were evaluated in the hippocampus prepared from the aged TG mice that had been injected by LPS at 4 h earlier (TG, $n = 5$).

Electrophysiology. Twenty-eight male C57BL/6 mice (WT and TG) of the following age groups: young (2–4 months of age; WT, $n = 6$; TG, $n = 5$) and aged (19–22 months of age; WT, $n = 10$; TG, $n = 7$) were used in the electrophysiological study. The brain was removed rapidly and hippocampal slices were prepared by cutting 400-μm-thick sagittal sections using a microslicer (VT1000S; Leica) as described previously (Hayashi et al., 2006). Some mice were injected LPS (0.33 mg/kg; Sigma-Aldrich) intraperitoneally 4 h before recording. Field EPSPs evoked by stimulation of the Schaffer collateral pathway were recorded from the CA1 subfield. LTP was induced by tetanus stimulation consisting of a train of pulses of 1 s duration given at 25, 50, and 100 Hz. All data were captured using the PowerLab (Molecular Devices), and then they were digitized (5–20 kHz) and stored on the hard disk of a personal computer for off-line analysis using the Scope software program.

Statistical analysis. Data are expressed as the mean ± SEM. The statistical analyses were performed by an ANOVA.

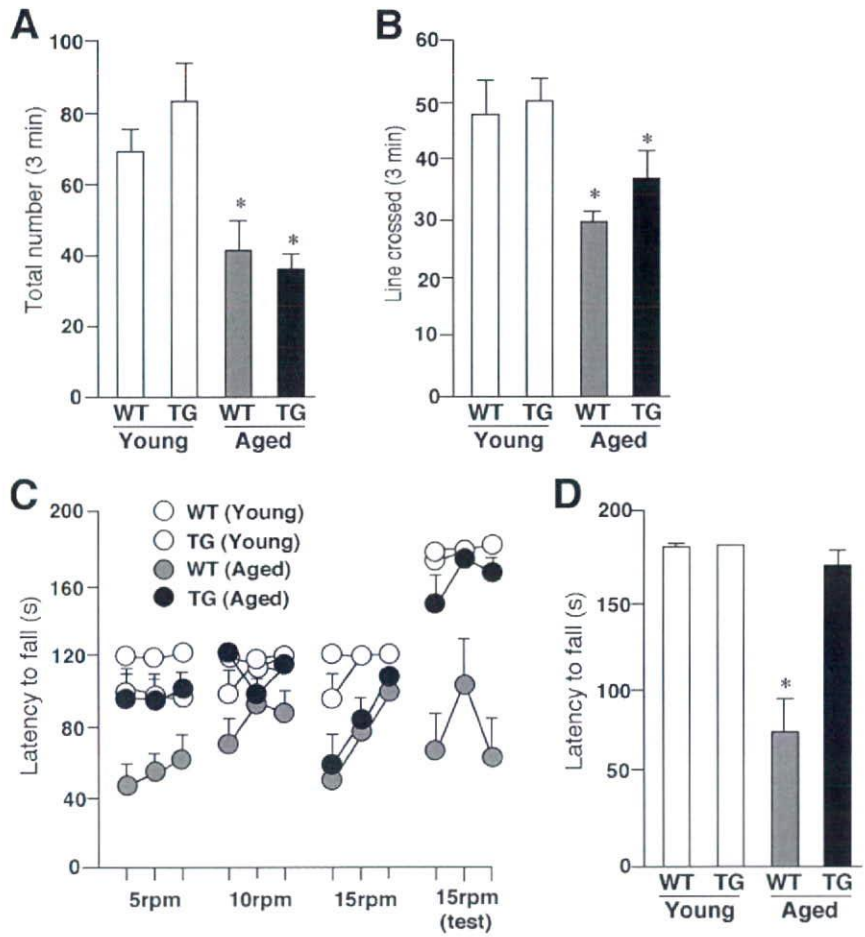

Figure 4. The amelioration of aged-dependent impairment of coordinated movements in the aged TG mice. ***A***, The mean total number of forepaw contacts. Each column and bar represent the mean ± SEM of six animals. The asterisks indicate significant differences versus the young group (*$p < 0.05$). ***B***, The mean incidence of line crossed. Each column and bar represent mean ± SEM of six animals. The asterisks indicate significant differences versus the young group (*$p < 0.05$). ***C***, The mean latency to fall from the rod given three practice trials at constant speed of 5 rpm in the first day, 10 and 15 rpm in the second day, and 15 rpm in the third (test) day. Each circle and bar represent the mean ± SEM of six animals. ***D***, The mean latency to fall from the rod in the test session (3 trials at 15 rpm). Each column and bar represents the mean ± SEM of six animals. An asterisk indicates a significant difference versus the young group (*$p < 0.05$).

Results

Inhibitory effect of TFAM overexpression on rotenone-induced intracellular ROS generation and NF-κB nuclear translocation in HeLa cells

TFAM overexpression may inhibit the ROS generation through reduction of mtDNA mutations, which subsequently retards the motor and memory functions. To elucidate this deduction, the effects of TFAM on intracellular ROS generation were first examined in HeLa cells overexpressing human TFAM using the tetracycline-off system. The protein level of TFAM in the HeLa cells increased approximately twofold by removal of DC, a derivative of tetracycline, from the culture medium (Fig. 1). Rotenone, an inhibitor of mitochondrial complex I, was used to produce ROS, which originated from the mitochondria, because impaired electrons transfer at complex I has been reported to be associated with an increased production of superoxide radicals (Hensley et al., 2000). Rotenone induced a significant increase in the oxidation level of DHE, a widely used ROS-sensitive dye (Fig. 2*A*,*B*). The mean oxidation level of rotenone-treated HeLa cells was significantly lower when cultured without DC than when cultured with DC. The effect of rotenone on the subsequent activation of NF-κB, a redox-sensitive nuclear transcription factor, was further examined in the HeLa cells overexpressing human TFAM by the tetracycline-off system. The activation of NF-κB in HeLa cells was assessed by visualizing its translocation from the cytoplasm to the nucleus after treatment with rotenone. Rotenone

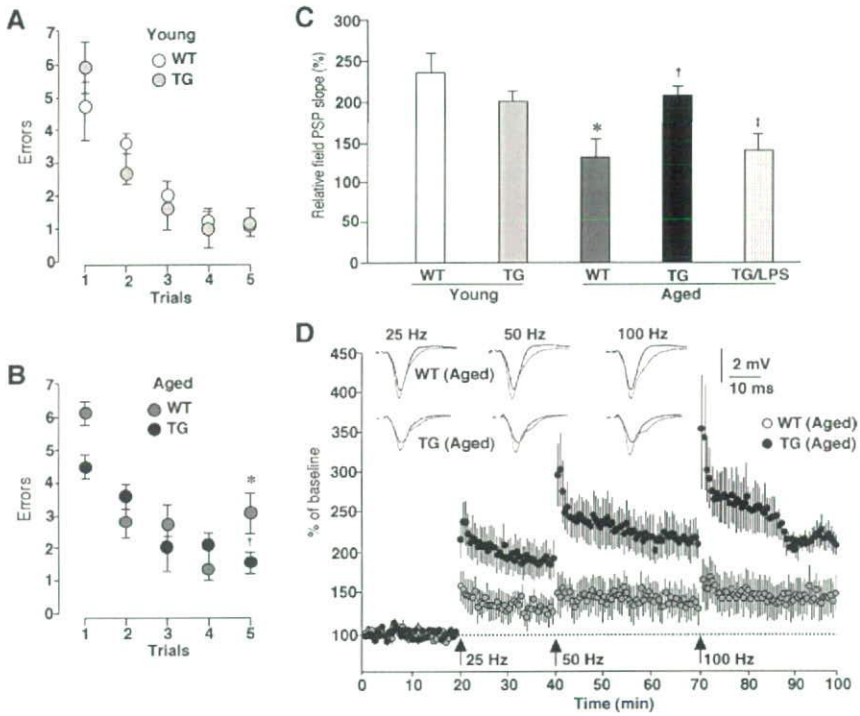

Figure 5. An amelioration of age-dependent decline of the working memory and the hippocampal LTP in the aged TG mice. ***A***, ***B***, The mean number of errors during radial-arm water maze performance in the TG and WT mice of both the young (***A***) and the aged groups (***B***). Four consecutive acquisition trials (trials 1–4) followed by a 30 min retention trial (trial 5) were conducted. Each circle and bar represents the mean ± SEM of six experiments. An asterisk indicates a significant difference versus the young WT mice ($^{*}p < 0.05$). A dagger indicates a significant difference versus the aged WT mice ($^{\dagger}p < 0.05$). ***C***, The mean relative EPSP slopes measured at 30 min after tetanic stimulation at 100 Hz in the Schaffer collateral–CA1 pathway of the WT and TG mice of both age groups and LPS-treated aged TG mice. Each column and bar represent the mean ± SEM of six slices from three animals in the young WT group, three slices from three animals in the young TG group, three slices from three animals in the aged WT group, 11 slices from seven animals in the aged TG group, and 15 slices from five animals in the aged TG group subjected to intraperitoneally injection of LPS (0.33 mg/kg) 4 h earlier. An asterisk indicates a significant difference versus the young WT mice ($^{*}p < 0.05$). A dagger indicates a significant difference versus the aged WT mice ($^{\dagger}p < 0.05$). A double dagger indicates a significant difference from the value of the aged TG mice ($^{\ddagger}p < 0.05$). ***D***, The cumulative potentiation of EPSP slope after consecutive tetanic stimulation at 25, 50, and 100 Hz in the hippocampus of aged WT and TG mice. Each circle and bar represent the mean ± SEM of three slices from three animals in the aged WT group, and 11 slices from seven animals in the aged TG group. The traces show the typical field EPSP before (black) and after stimulation at each frequency (gray).

also induced the NF-κB nuclear translocation in HeLa cells cultured with DC. However, the mean ratio of translocated NF-κB in rotenone-treated HeLa cells was significantly lower when they were cultured without DC than when they were cultured with DC (Fig. 2*C*;*D*, arrowheads). These results clearly indicate that the overexpression of TFAM prevents the overproduction of ROS originated from the mitochondria and inhibits the intracellular redox-sensitive signaling of NF-κB.

Amelioration of age-dependent increased oxidative stress and reduced activity of mitochondrial respiratory enzymes in the brain of aged TG mice

Next, the effect of TFAM overexpression on the ROS generation in the brain was examined using TG mice and their wild-type littermates. In the young TG mice, the human TFAM protein was expressed in the soluble extracts prepared from the whole brain, without any significant changes in the expression of the endogenous mouse Tfam protein (Fig. 3*A*). Immunostaining also showed human TFAM to be expressed in both neurons and glial cells in the brain parenchyma of the TG mice (Fig. 3*B*). Lipid peroxidation, which was indicated by TBARS, significantly increased in the brain tissue specimens of the aged WT mice. The increased lipid peroxidation may therefore contribute to the senescent changes in the brain functions. However, the mean TBARS level in the brain tissues of the aged TG mice was significantly lower than that in the aged WT mice and comparable with that in the young group (Fig. 3*C*). Many studies have suggested a mechanistic link between mtDNA mutations, a loss of mitochondrial respiratory enzyme functions, and generation of ROS from the mitochondria. A decreased electron transfer activity has been observed in the mitochondria of experimental animals on aging (Navarro et al., 2005; Mao et al., 2006). The activity of complexes I and IV in the mitochondrial fractions prepared from the brain tissue specimens of the aged WT mice were significantly lower compared with the young WT mice, whereas those of complexes II and III were unaffected (Fig. 3*D*). These results are consistent with those of previous reports (Navarro et al., 2005; Mao et al., 2006). In the brain tissue specimens prepared from the TG mice, however, there was no age-dependent reduction in activity for any of the complexes (Fig. 3*D*). Therefore, the age-dependent decrease in enzymatic activities of complexes I and IV could be mainly a consequence of oxidative mtDNA damage. Furthermore, it is reasonable to consider that human TFAM effectively counteracted this oxidative mtDNA damage to rescue the age-dependent decrease in mitochondrial complex enzymatic activities.

Amelioration of the aged-dependent impairment of motor learning and memory in aged TG mice

The effects of TFAM overexpression were next observed regarding the age-dependent impairment of the locomotor activity and the motor learning and memory using rotarod tests, because ROS are considered to be a major causal factor for the progressive age-dependent motor and learning functions.

The locomotor activities were measured by both the cylinder and line-crossing tests. The mean total number of both forepaw contacts and the incidence of line crossed significantly decreased with aging in both the WT and TG mice (Fig. 4*A*,*B*). The mean total number of forepaw contacts showed no significant difference between the aged WT mice and the aged TG mice (Fig. 4*A*). All groups of animals used in this study had an equal forelimb use. The mean total incidence of line crossed in the aged TG mice was larger than that in the aged WT mice, whereas the difference did not reach the statistical significance (Fig. 4*B*).

Next, the rotarod test was used to examine the effects of TFAM overexpression on the age-dependent impaired acquisition of skilled behavior. With the fixed speed rotarod protocol, both the young WT and TG mice could rapidly acquire the necessary skilled behavior on the rotating rod to prevent a fall. They were able to stay on the rod for the maximum time at both trained at speeds between 5 and 15 rpm and tested at 15 rpm (Fig. 4*C*). The aged WT mice showed an increase in the latency to fall across trials, but their score was much lower than that of the young

group. During the test session, the average time spent on the rod significantly decreased with aging in the WT mice (Fig. 4*D*). Furthermore, regardless of the progress during three trials at 15 rpm, the aged WT mice fell down from the rod in ~60 s in the first trial in the test session on the next day (Fig. 4*C*,*D*). However, the aged TG mice could rapidly acquire the skilled behavior on the rotating rod similar to the young group at speeds with 5 and 10 rpm (Fig. 4*C*). In the task at a speed of 15 rpm, the aged TG mice showed a slow acquisition of the skilled behavior compared with the young group. Because of the fact that the mice had to turn their position against the direction of rotation and progress forward to maintain their equilibrium on the rod after the rod started to rotate, they needed to acquire the more skillful behavior at higher speeds. During the test session, however, the mean latency to fall of the aged TG mice significantly increased compared with that of the aged WT mice (Fig. 4*D*). Although the aged WT animals could not reach the maximum time during the test session for their low endurance, they stayed on the rod for more than their maximum time during the fixed speed protocol and at speed >15 rpm in the accelerating rotarod protocol (accelerate continuously from 4 to 40 rpm over 300 s) (data not shown). In addition, there was no difference in locomotive activation between WT and TG mice (Fig. 4*A*,*B*), thus suggesting that a decrease in the time spent on the rod was caused by an impairment of the acquisition of the skilled behavior rather than by a decline in their endurance or motivation. These results indicate that the age-dependent motor memory impairment markedly improved in the TG mice.

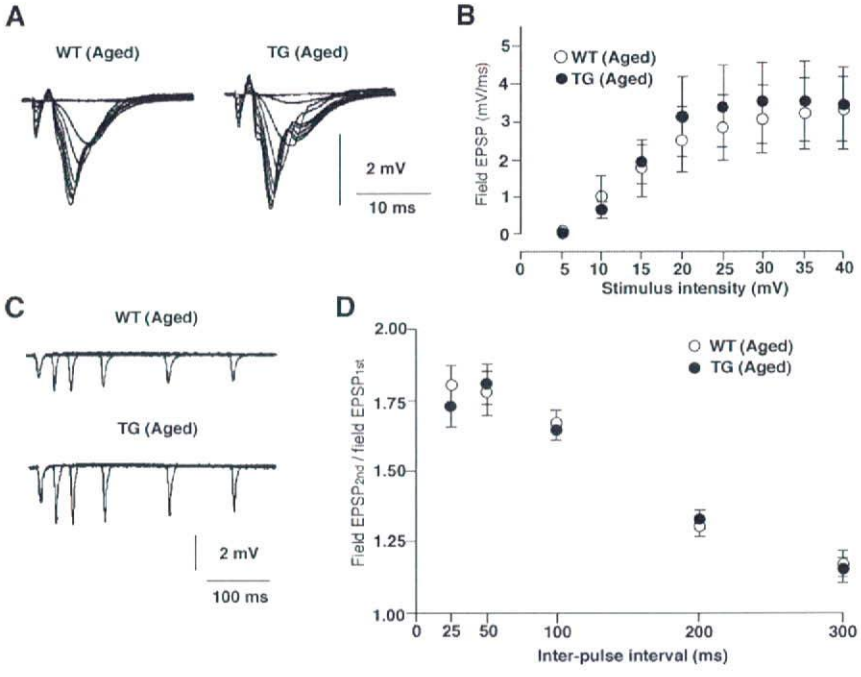

Figure 6. Effects of TFAM overexpression on basal synaptic transmission in the hippocampus. ***A***, Superimposed traces of field EPSPs evoked by different stimulus intensities (5–40 V) from the CA1 subfield of hippocampal slices prepared from the aged WT and TG mice. ***B***, The input–output relationship for the mean field EPSP slope plotted against stimulus intensity in the Schaffer collateral–CA1 synapses. Open circles, WT mice; filled circles, TG mice. The point and bar represent the mean and SEM of eight slices from eight animals in the aged WT group, and seven slices from three animals in the aged TG group. No significant difference was observed between the WT and TG slices. ***C***, Superimposed traces of field EPSPs evoked by paired pulse stimulation of the stratum radiatum with five different interspike intervals in the CA1 subfield of hippocampal slices prepared from the aged WT and TG mice. ***D***, The plots of the relative amplitude of the second stimulation to the first responses against various interstimulus intervals. Open circles, WT mice; filled circles, TG mice. The point and bar represent the mean and SEM of six to eight slices from six animals in the aged WT mice, and seven slices from seven animals in aged TG mice. No significant difference was observed between WT and TG slices.

Amelioration of the age-dependent decline of the working memory and the hippocampal LTP in the aged TG mice

Next, the effects of TFAM overexpression on the age-dependent impairment of the working memory were examined using the radial arm water maze, which combines elements of a radial-arm maze and a water maze (Morgan et al., 2000). Both the WT and TG mice of the young group showed an average of four to six errors in the first trial and only one error in the retention trial (trial 5) (Fig. 5*A*). In both the WT and TG mice of the aged group, the animals showed four to six errors on the first trial. On the retention trial (trial 5), the mean number of errors in the aged TG mice was significantly lower than that in the aged group and it was comparable with that in the young group (Fig. 5*B*).

These observations prompted the additional examination of the effects of TFAM overexpression on the age-dependent decline in the hippocampal LTP, which is postulated to be a cellular substrate for hippocampus-dependent memory. The LTP experiments were performed on transverse hippocampal slices as described previously (Tomimatsu et al., 2002; Hayashi et al., 2006). The cumulative potentiation of the field EPSP slope was measured after consecutive tetanic stimulation at 25, 50, and 100 Hz. When the relative field EPSP slope was measured at 30 min after tetanic stimulation with 100 Hz, there was no significant difference in the mean magnitude of LTP in the Schaffer collateral–CA1 pathway between the young WT and TG mice (Fig. 5*C*). Consistent with previous studies (Okada et al., 1995), LTP in the Schaffer collateral–CA1 pathway was significantly lower in the aged WT mice than in the young WT mice (Fig. 5*C*). However, LTP was induced by conditioned stimuli even at a relatively low frequency (25 or 50 Hz) in the aged TG mice (Fig. 5*D*). The mean relative field EPSP slope measured at 30 min after tetanic stimulation with 100 Hz in the aged TG mice was significantly greater than that in the aged WT mice and it was also comparable with that in the young group (Fig. 5*C*,*D*).

However, there was no significant difference in either the basal synaptic transmission (Fig. 6*A*,*B*) or the paired-pulse facilitation (Fig. 6*C*,*D*) between the aged WT and TG mice. These results clearly indicate that an overexpression of TFAM significantly ameliorates the age-dependent deficits in the working memory and the hippocampal LTP.

Amelioration of increased oxidation and inflammation in the brain of the aged TG mice

ROS have been associated with normal aging and age-dependent neurodegenerative disorders (Watson et al., 2006). The localization of oxidative damages was examined in the hippocampus and other brain regions. The immunoreactivity for HNE and 8-oxo-dG, which are formed by oxidant interactions with lipids and DNA, respectively, increased in the aged WT mouse brains. In-

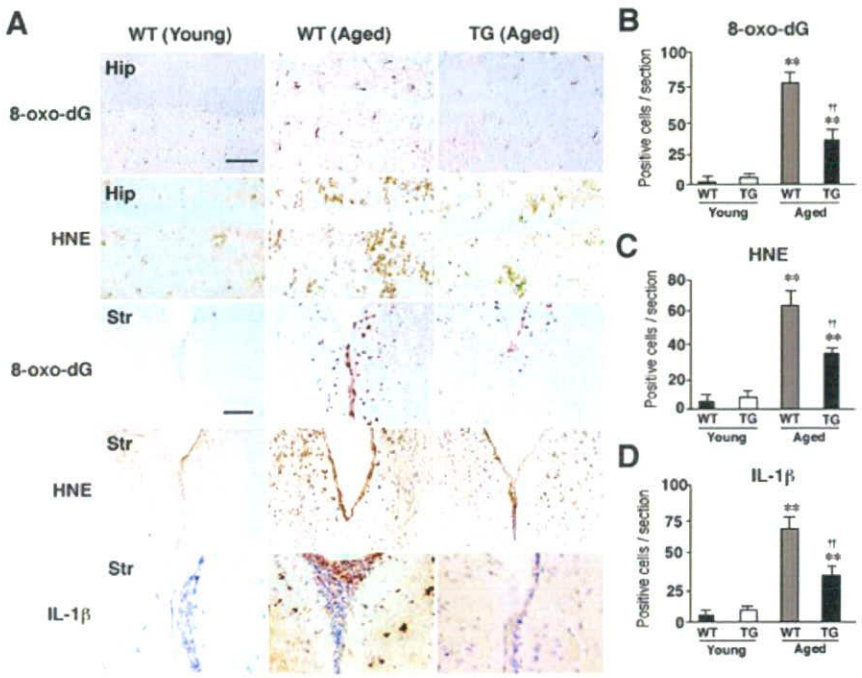

Figure 7. Amelioration of ROS-mediated oxidation of cell components and inflammation in the hippocampus of the aged TG mice. ***A***, Immunohistochemical staining for 8-oxo-dG and HNE in the CA1 hippocampal subfield (Hip) and the periventricular area of the striatum (Str) of the young WT, the aged WT, and the aged TG mice. Scale bars, 50 μm. ***B–D***, The mean number of positive cells for 8-oxo-dG (***B***), HNE (***C***), and IL-1β/cells (***D***) in the hippocampal CA1 subfield of the WT, the TG, and the LPS-treated TG mice of the aged group. Each column and bar represent the mean ± SEM of nine sections from three animals. The asterisks indicate significant differences versus the young group (**$p < 0.01$). The daggers indicate significant differences versus the aged WT mice ($^{\dagger\dagger}p < 0.01$).

creased immunoreactivity was prominent especially in the hippocampus and the periventricular areas of the striatum (Fig. 7*A–C*). In contrast, the immunoreactivity of these markers for oxidative stress was barely detectable in the brain parenchyma of the aged TG mice (Fig. 7*A–C*). The immunoreactivity for IL-1β also significantly increased in the periventricular areas (Fig. 7*A*,*D*) and the hippocampus (data not shown) of the aged WT mice but not those brain regions of the aged TG mice. Double immunofluorescence staining was performed to elucidate the cellular sources for 8-oxo-dG, HNE, and IL-1β. Rather surprisingly, the immunoreactivity for both 8-oxo-dG and HNE corresponded closely with microglia exhibiting activated morphology and partially with neurons, but not with astrocytes localized in the periventricular area of the aged WT mice (Fig. 8*A*,*B*). The relatively intense immunoreactivity for IL-1β corresponded well with that for both Iba1 and GFAP, but not MAP2 in the periventricular areas (Fig. 8*C*) and the hippocampus (Fig. 9*C*) of the aged WT mice. In the hippocampus of the aged WT mice, the immunoreactivity for either 8-oxo-dG (Fig. 8*D*, red) or HNE (data not shown) was found mainly in glial cells and only partially in neurons that were intensely stained with YOYO-1 (green). The immunoreactivity for 8-oxo-dG (Fig. 8*F*) and HNE (Fig. 8*G*) found in the stratum radiatum corresponded well with microglia. However, the immunoreactivity for either 8-oxo-dG (Fig. 8*E*) or HNE (data not shown) was barely detectable in the hippocampus of the aged TG mice.

Recent accumulating evidence indicates that intracellular ROS is capable of activating redox-dependent signal transduction cascades and transcription factors including NF-κB and mitogen-activated protein (MAP) kinases in various cell types including microglia (Pawate et al., 2004; Yamasaki et al., 2007). The activation of NF-κB and MAP kinases is closely associated with the expression of inflammatory mediators including IL-1β in microglia. Furthermore, inflammatory mediators including IL-1β secreted from microglia have been recently reported to play a pivotal role in the attenuation of the working memory (Gemma et al., 2005) and the hippocampal LTP in aged rats (Griffin et al., 2006). Therefore, the relationship between the oxidative damage of mtDNA, the expression level of IL-1β, and the magnitude of the hippocampal LTP was examined by treatment with LPS, which is known to increase the generation of mitochondrial ROS (Woo et al., 2004; Emre et al., 2007). At 4 h after the systemic injection of LPS, the mean level of IL-1β in the whole brain of the aged TG mice significantly increased, thus reaching a similar level to that of the aged WT mice (Fig. 9*A*,*B*). However, the mean level of IL-1β in the whole brain of the LPS-treated aged TG mice was significantly lower that of the LPS-treated aged WT mice (Fig. 9*A*,*B*). However, the immunoreactivity for 8-oxo-dG corresponded closely with that for Cyt *b*, a marker for the mitochondria, was observed in the hippocampus of the aged WT mice. In contrast, there was slight immunoreactivity for either IL-1β or 8-oxo-dG in the hippocampus of the aged TG mice. On treatment with LPS, the immunoreactivity for both IL-1β and 8-oxo-dG markedly increased in the hippocampus of the aged TG mice (Fig. 9*C*). The immunoreactive products for IL-1β showed a specked appearance, thus suggesting the localization of IL-1β in lysosomes where IL-1β colocalizes with lysosomal enzymes (Gardella et al., 2001; Qu et al., 2007). The mean immunofluorescence intensity of IL-1β/cell in the hippocampus of the LPS-treated aged TG mice was significantly higher than that in the aged TG mice and it was also comparable with that in the aged WT mice (Fig. 9*C*,*D*). At the same time, the mean immunofluorescence intensity of 8-oxo-dG/mitochondria in the hippocampus of the LPS-treated aged TG mice was also significantly higher than that in the aged TG mice (Fig. 9*C*,*E*). Finally, LTP in the Schaffer collateral–CA1 pathway was measured in hippocampal slices prepared from the LPS-treated aged TG mice. As shown in Figure 5*C*, the mean magnitude of LTP in the LPS-treated aged TG mice was significantly lower than that of none-treated aged TG mice (143.86 ± 10.17%; $p < 0.05$).

These observations strongly suggest that overexpressed human TFAM also significantly suppressed mitochondrial ROS generation and the subsequent IL-1β production by microglia in the brain. Furthermore, the magnitude of the hippocampal LTP was inversely correlated with the expression level of IL-1β and the severity of mtDNA damage in microglia.

Discussion

The mitochondrial theory of aging states that the original damage to mtDNA is induced by the continuous production of ROS (Beckman and Ames, 1998; Harman, 2006). The most important

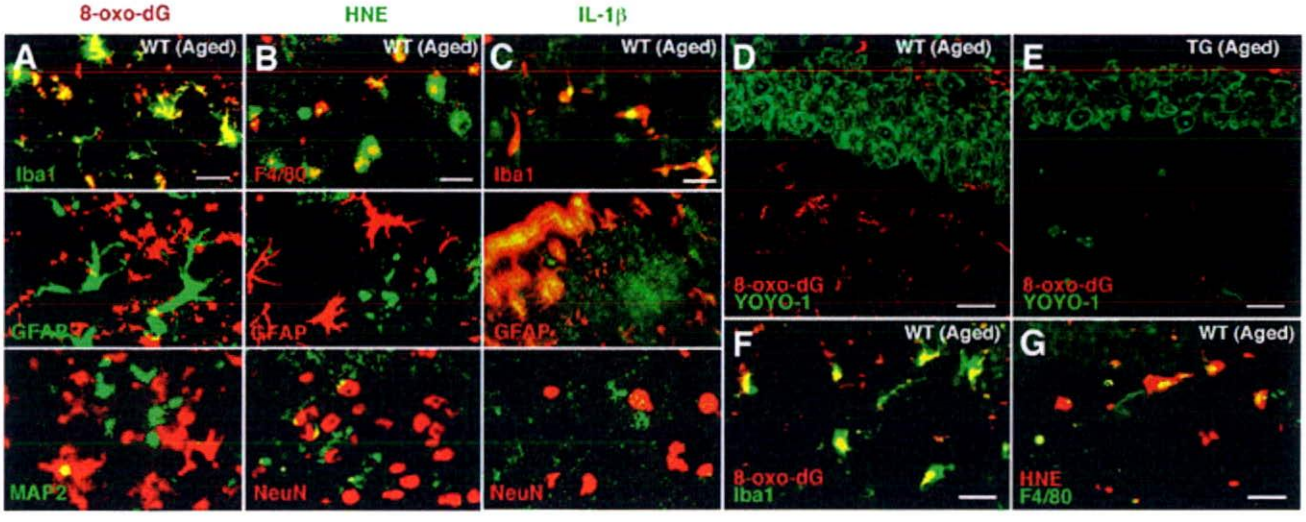

Figure 8. Immunofluorescent CLSM images for 8-oxo-dG, HNE, and IL-1β in the striatum and the hippocampus. ***A–C***, Immunofluorescence for 8-oxo-dG (***A***), HNE (***B***), and IL-1β (***C***) with cell type markers (Iba1, F4/80 for microglia, GFAP for astrocytes, MAP2 and NeuN for neurons) in the periventricular area of the striatum of the aged WT mice. Scale bars: ***A–C***, 30 μm. ***D***, ***E***, Immunofluorescence for 8-oxo-dG (red) with YOYO-1-stained neurons (green) in the hippocampal CA1 subfield of the aged WT (***D***) and TG (***E***) mice. Scale bars: ***D***, ***E***, 20 μm. ***F***, ***G***, Immunofluorescence for 8-oxo-dG (***F***) and HNE (***G***) with markers of microglia (Iba1 and F4/80) in the hippocampal CA1 subfield of the aged WT mice. Scale bars: ***F***, ***G***, 5 μm.

finding in the current study is that the overexpression of human TFAM reduced age-dependent oxidative damages of mtDNA mainly in microglia, thus preventing the age-dependent impairments in the motor and working memories in mice. These beneficial effects of human TFAM overexpression were attributable to functional improvements in the brain but not in the musculature in the aged TG mice. Considering (1) the abundance of TFAM, (2) the structure of TFAM as high-mobility group DNA-binding protein, and (3) the association of TFAM with mtDNA protein complexes (Alam et al., 2003; Kanki et al., 2004a; Kang and Hamasaki, 2005), (4) human TFAM dose not appear to work as a transcription factor in a mouse cell (Ohgaki et al., 2007), human TFAM can cover the whole region of a mtDNA forming nucleoid to protect it from oxidative modifications or additional damage without modulation of gene expression (Kanki et al., 2004a; Kang and Hamasaki, 2005). The present study clearly demonstrated a causal relationship among mitochondrial ROS, mitochondrial dysfunction, and deficits in the brain functions during the process of aging.

The results of this study revealed that microglia are the main cellular source of oxidation products including HNE and 8-oxo-dG in the brain of the WT mice. It was also noted that the accumulation of oxidation products in microglia was more marked in specific brain areas including the hippocampus and the periventricular area of the striatum. These marked oxidative stresses on microglia in the hippocampus and striatum are considered to be closely associated with the age-dependent memory deficits, because these brain regions play key roles in the formation of motor and working memories, respectively (Morris et al., 1982; Albin et al., 1989). These observations remain, however, somewhat puzzling because the most severe age-dependent mtDNA injury and greatest ROS production in the brain are believed to occur in neurons that are long-living postmitotic cells. Liu et al. (2002) demonstrated RNA to be the predominant oxidized neuronal nucleic acid in the aged rat brain. Therefore, RNA being the predominant oxidized neuronal nucleic acid in the aged animal brain may explain the paucity of oxidative mtDNA damage in neurons of the aged WT mice in the present immunohistochemical analysis using anti-8-oxo-dG antibody. However, some evidence suggests that the mitochondrial turnover in microglia is extremely slow and that abundant damaged mitochondria, which can generate excessive ROS, may accumulate in microglia. A recent study showed the subunit c of the mitochondrial ATP synthase complex to accumulate most intensively in microglia in the brain of the mice deficient for cathepsin D, which is a protease responsible for proteolytic degradation of subunit c (Yamasaki et al., 2007). Furthermore, Lawson et al. (1992) revealed a slow microglial turnover in the normal adult mouse brain, although microglia are replaceable cells. The age-dependent changes in the mitochondrial functions and ROS production in microglia are thus expected to be elucidated in future studies.

The current observations showed that TFAM overexpression suppressed the ROS generation induced by rotenone and the subsequent activation of NF-κB in HeLa cells. ROS induced by rotenone were generated from the mitochondria because an impaired electron transfer at complex I is associated with an increased production of ROS in the mitochondria (Schönfeld and Reiser, 2006). Furthermore, a decrease in the enzymatic activity of complex I in the range of 16–30% is sufficient to stimulate mitochondrial ROS generation (Sipos et al., 2003). Therefore, a decrease in the activity of both complexes I and IV by approximately one-third in the brain of the aged WT mice could induce excessive mitochondrial ROS generation. These excess ROS may further cause oxidative DNA damage, lipid peroxidation, and IL-1β production through activation of NF-κB. Therefore, human TFAM overexpression may also reduce excessive mitochondrial ROS generation in the brain during aging and the subsequent oxidative damage and inflammatory responses through the protection of mtDNA against oxidative injury.

Although the observations noted herein showed that the systemic injection of LPS could further activate microglia to produce IL-1β in the brain of the aged TG mice, the mean amount of IL-1β in the brain of the LPS-treated aged TG mice was significantly lower than that of the LPS-treated aged WT mice. LPS is therefore suggested to activate microglia by a multitude of receptors and interacting pathways (Qin et al., 2005), with the production of ROS. Recently, mitochondria have been found to contribute to LPS-induced ROS signaling in macrophages (Woo et al.,

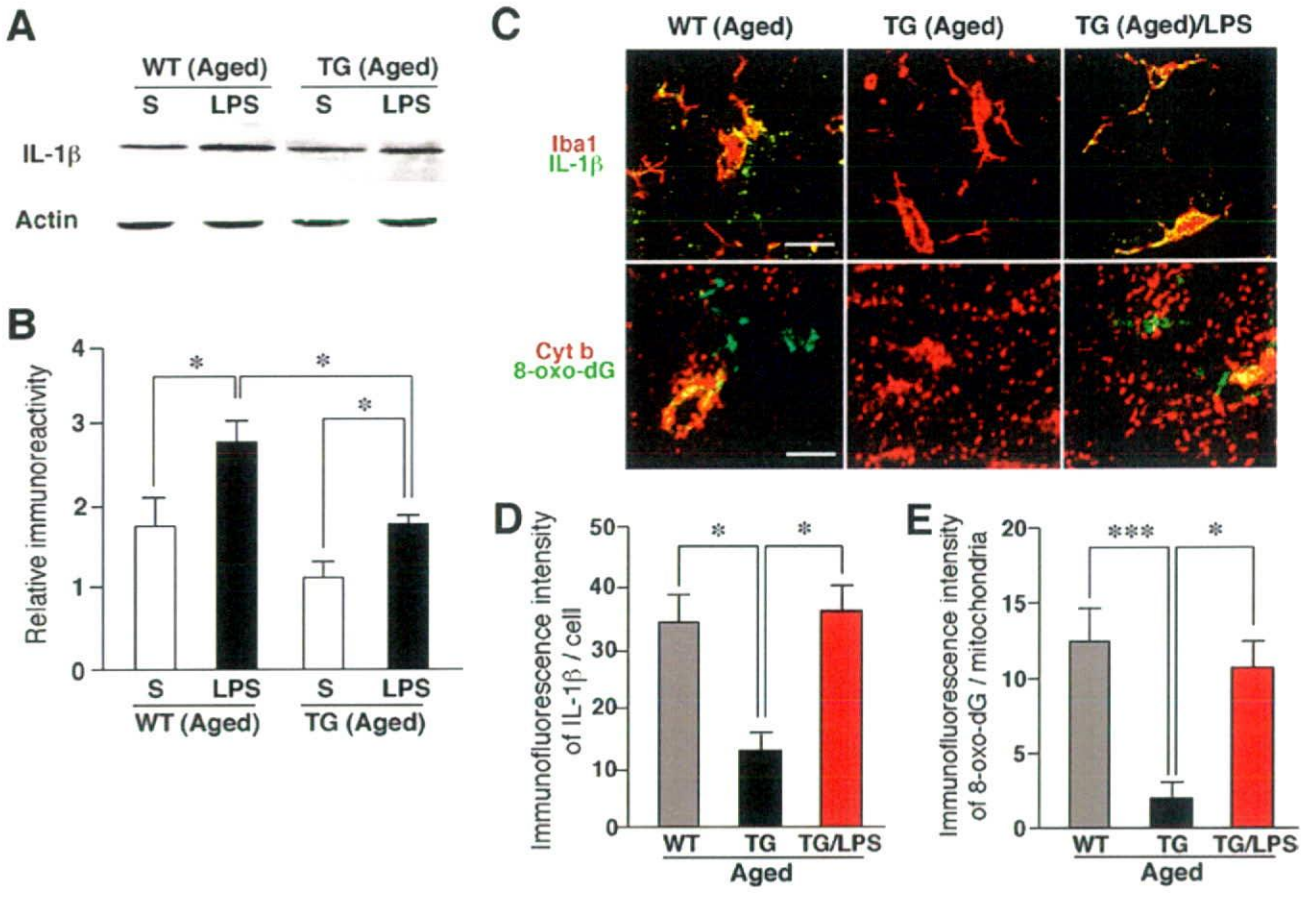

Figure 9. Increased expression of IL-1β in the hippocampus after the systemic injection of LPS and the inhibitory effect of the TFAM overexpression. ***A***, Immunoblot analysis of IL-1β in the whole brain of the aged WT and TG mice subjected to intraperitoneal injection of saline (S) or LPS (0.33 mg/kg) 4 h earlier. ***B***, The mean protein level of IL-1β. The mean relative immunoreactivity was determined using the level of actin as an internal control. Each column and bar represent the mean and SEM of three experiments, respectively. The asterisks indicate significant differences between the values (*$p < 0.05$). ***C***, Immunofluorescent CLSM images for IL-1β (green) with the microglial marker Iba1 (red; top row), and 8-oxo-dG (green) with the mitochondrial marker Cyt *b* (red; bottom row) in the hippocampal CA1 subfield of the aged WT, the aged TG, and the LPS-treated aged TG mice. Scale bars: top row, 10 μm; bottom row, 5 μm. ***D***, The mean immunofluorescence intensity of IL-1β/cell in the hippocampal CA1 subfield of the WT, the TG, and the LPS-treated TG mice of the aged group. Each column and bar represent the mean ± SEM of nine sections from three animals. The asterisks indicate significant differences between the values (*$p < 0.05$). ***E***, The mean immunofluorescence intensity of 8-oxo-dG/mitochondria in the hippocampal CA1 subfield of the WT, the TG, and the LPS-treated TG mice of the aged group. Each column and bar represent the mean ± SEM of seven sections from two animals. The asterisks indicate significant differences between the values (***$p < 0.0001$; *$p < 0.05$).

2004; Emre et al., 2007). It is therefore conceivable that the overexpression of TFAM also inhibited the LPS-induced mitochondrial ROS generation to reduce oxidative mtDNA damage and the IL-1β levels in the brain. There is increasing evidence that neuroinflammation mediated by activated microglia plays a major causative role in age-dependent deficit of the working memory (Gemma et al., 2005) and the hippocampal LTP (Griffin et al., 2006). It is therefore reasonable to consider that TFAM overexpression may inhibit any excessive ROS generation caused by a reduced mitochondrial respiratory chain enzymatic activity in microglia during aging, because ROS can activate NF-κB, which integrates oxidative stress and the inflammatory pathways (Pawate et al., 2004). Additional clarification of the mechanisms by which TFAM exhibits an antioxidant effect and maintains the mitochondrial function may eventually lead to the development of an antiaging strategy to preserve the brain functions.

References

Alam TI, Kanki T, Muta T, Ukaji K, Abe Y, Nakayama H, Takio K, Hamasaki N, Kang D (2003) Human mitochondrial DNA is packaged with TFAM. Nucleic Acids Res 31:1640–1645.

Albin RL, Young AB, Penney JB (1989) The functional anatomy of basal ganglia disorders. Trends Neurosci 12:366–375.

Beckman KB, Ames BN (1998) The free radical theory of aging matures. Physiol Rev 78:547–581.

Corral-Debrinski M, Horton T, Lott MT, Shoffner JM, Beal MF, Wallace DC (1992) Mitochondrial DNA deletions in human brain: regional variability and increase with advanced age. Nat Genet 2:324–329.

Emre Y, Hurtaud C, Nübel T, Criscuolo F, Ricquier D, Cassard-Doulcier AM (2007) Mitochondria contribute to LPS-induced MAPK activation via uncoupling protein UCP2 in macrophages. Biochem J 402:271–278.

Forster MJ, Dubey A, Dawson KM, Stutts WA, Lal H, Sohal RS (1996) Age-related losses of cognitive function and motor skills in mice are associated with oxidative protein damage in the brain. Proc Natl Acad Sci U S A 93:4765–4769.

Gardella S, Andrei C, Lotti LV, Poggi A, Torrisi MR, Zocchi MR, Rubartelli A (2001) $CD8^+$ T lymphocytes induce polarized exocytosis of secretory lysosomes by dendritic cells with release of interleukin-1β and cathepsin D. Blood 98:2152–2159.

Gemma C, Fister M, Hudson C, Bickford PC (2005) Improvement of memory for context by inhibition of caspase-1 in aged rats. Eur J Neurosci 22:1751–1756.

Griffin R, Nally R, Nolan Y, McCartney Y, Linden J, Lynch MA (2006) The

age-related attenuation in long-term potentiation is associated with microglial activation. J Neurochem 99:1263–1272.

Harman D (2006) Free radical theory of aging: an update: increasing the functional life span. Ann N Y Acad Sci 1067:10–21.

Hayashi Y, Tomimatsu Y, Suzuki H, Yamada J, Wu Z, Yao H, Kagamiishi Y, Tateishi N, Sawada M, Nakanishi H (2006) The intra-arterial injection of microglia protects hippocampal CA1 neurons against global ischemia-induced functional deficits in rats. Neuroscience 142:87–96.

Hensley K, Kotake Y, Sang H, Pye QN, Wallis GL, Kolker LM, Tabatabaie T, Stewart CA, Konishi Y, Nakae D, Floyd RA (2000) Dietary choline restriction causes complex I dysfunction and increased H_2O_2 generation in liver mitochondria. Carcinogenesis 21:983–989.

Iancu R, Mohapel P, Brundin P, Paul G (2005) Behavioral characterization of a unilateral 6-OHDA-lesion model of Parkinson's disease in mice. Behav Brain Res 162:1–10.

Ide T, Tsutsui H, Kinugawa S, Utsumi H, Kang D, Hattori N, Uchida K, Arimura K, Egashira K, Takeshita A (1999) Mitochondrial electron transport complex I is a potential source of oxygen free radicals in the failing myocardium. Circ Res 85:357–363.

Ikeuchi M, Matsusaka H, Kang D, Matsushima S, Ide T, Kubota T, Fujiwara T, Hamasaki N, Takeshita A, Sunagawa K, Tsutsui H (2005) Overexpression of mitochondrial transcription factor A ameliorates mitochondrial deficiencies and cardiac failure after myocardial infarction. Circulation 112:683–690.

Kajitani K, Yamaguchi H, Dan Y, Furuichi M, Kang D, Nakabeppu Y (2006) MTH1, an oxidized purine nucleoside triphosphatase, suppresses the accumulation of oxidative damage of nucleic acids in the hippocampal microglia during kainate-induced excitotoxicity. J Neurosci 26:1688–1698.

Kang D, Hamasaki N (2005) Mitochondrial transcription factor A in the maintenance of mitochondrial DNA: overview of its multiple roles. Ann N Y Acad Sci 1042:101–108.

Kanki T, Nakayama H, Sasaki N, Takio K, Alam TI, Hamasaki N, Kang D (2004a) Mitochondrial nucleoid and transcription factor A. Ann N Y Acad Sci 1011:61–68.

Kanki T, Ohgaki K, Gaspari M, Gustafsson CM, Fukuoh A, Sasaki N, Hamasaki N, Kang D (2004b) Architectural role of mitochondrial transcription factor A in maintenance of human mitochondrial DNA. Mol Cell Biol 24:9823–9834.

Lawson LJ, Perry VH, Gordon S (1992) Turnover of resident microglia in the normal adult mouse brain. Neuroscience 48:405–415.

Lin MT, Simon DK, Ahn CH, Kim LM, Beal MF (2002) High aggregate burden of somatic mtDNA point mutations in aging and Alzheimer's disease brain. Hum Mol Genet 11:133–145.

Liu J, Head E, Gharib AM, Yuan W, Ingersoll RT, Hagen TM, Cotman CW, Ames BN (2002) Memory loss in old rats is associated with brain mitochondrial decay and RNA/DNA oxidation: partial reversal by feeding acetyl-L-carnitine and/ or R-α-lipoic acid. Proc Natl Acad Sci U S A 99:2356–2361.

Mao L, Zabel C, Wacker MA, Nebrich G, Sagi D, Schrade P, Bachmann S, Kowald A, Klose J (2006) Estimation of the mtDNA mutation rate in aging mice by proteome analysis and mathematical modeling. Exp Gerontol 41:11–24.

Morgan D, Diamond DM, Gottschall PE, Ugen KE, Dickey C, Hardy J, Duff K, Jantzen P, DiCarlo G, Wilcock D, Connor K, Hatcher J, Hope C, Gordon M, Arendash GW (2000) Aβ peptide vaccination prevents memory loss in an animal model of Alzheimer's disease. Nature 408:982–985.

Morris RG, Garrud P, Rawlins JN, O'Keefe J (1982) Place navigation impaired in rats with hippocampus lesions. Nature 297:681–683.

Navarro A, Sánchez Del Pino MJ, Gómez C, Peralta JL, Boveris A (2002) Behavioral dysfunction, brain oxidative stress, and impaired mitochondrial electron transfer in aging mice. Am J Physiol Regul Integr Comp Physiol 282:R985–R992.

Navarro A, Gomez C, López-Cepero JM, Boveris A (2004) Beneficial effects of moderate exercise on mice aging: survival, behavior, oxidative stress, and mitochondrial electron transfer. Am J Physiol Regul Integr Comp Physiol 286:R505–R511.

Navarro A, Gómez C, Sánchez-Pino MJ, González H, Bández MJ, Boveris AD, Boveris A (2005) Vitamin E at high doses improves survival, neurological performance, and brain mitochondrial function in aging male mice. Am J Physiol Regul Integr Comp Physiol 289:R1329–R1399.

Ohgaki K, Kanki T, Fukuoh A, Kurisaki H, Aoki Y, Ikeuchi M, Kim SH, Hamasaki N, Kang D (2007) The C-terminal tail of mitochondrial transcription factor A markedly strengthens its general binding to DNA. J Biochem 141:201–211.

Okada M, Nakanishi H, Tamura A, Urae A, Mine K, Yamamoto K, Fujiwara M (1995) Long-term spatial cognitive impairment after middle cerebral artery occlusion in rats: no involvement of the hippocampus. J Cereb Blood Flow Metab 15:1012–1021.

Parisi MA, Clayton DA (1991) Similarity of human mitochondrial transcription factor 1 to high mobility group proteins. Science 252:965–969.

Pawate S, Shen Q, Fan F, Bhat NR (2004) Redox regulation of glial inflammatory response to lipopolysaccharide and interferon γ. J Neurosci Res 77:540–551.

Qin L, Li G, Qian X, Liu Y, Wu X, Liu B, Hong JS, Block ML (2005) Interactive role of the Toll-like receptor 4 and reactive oxygen species in LPS-induced microglia activation. Glia 52:78–84.

Qu Y, Franchi L, Nunez G, Dubyak GR (2007) Nonclassical IL-1β secretion stimulated P2X7 receptors is dependent on inflammasome activation and correlated with exosome release in murine macrophages. J Immunol 179:1913–1925.

Schönfeld P, Reiser G (2006) Rotenone-like action of the branched-chain phytanic acid induces oxidative stress in mitochondria. J Biol Chem 281:7136–7142.

Sipos I, Tretter L, Adam-Vizi V (2003) Quantitative relationship between inhibition of respiratory complexes and formation of reactive oxygen species in isolated nerve terminals. J Neurochem 84:112–118.

Tillerson JL, Cohen AD, Caudle WM, Zigmond MJ, Schallert T, Miller GW (2002) Forced nonuse in unilateral parkinsonian rats exacerbates injury. J Neurosci 22:6790–6799.

Tomimatsu Y, Idemoto S, Moriguchi S, Watanabe S, Nakanishi H (2002) Proteases involved in long-term potentiation. Life Sci 72:355–361.

Watson JB, Arnold MM, Ho YS, O'Dell TJ (2006) Age-dependent modulation of hippocampal long-term potentiation by antioxidant enzymes. J Neurosci Res 84:1564–1574.

Woo CH, Lim JH, Kim JH (2004) Lipopolysaccharide induces matrix metalloproteinase-9 expression via a mitochondrial reactive oxygen species-p38 kinase-activator protein-1 pathway in raw 264.7 cells. J Immunol 173:6973–6980.

Yamasaki R, Zhang J, Koshiishi I, Sastradipura Suniarti DF, Wu Z, Peters C, Schwake M, Uchiyama Y, Kira J, Saftig P, Utsumi H, Nakanishi H (2007) Involvement of lysosomal storage-induced p38 MAP kinase activation in the overproduction of nitric oxide by microglia in cathepsin D-deficient mice. Mol Cell Neurosci 35:573–584.

Am J Physiol Heart Circ Physiol 295: H1081–H1089, 2008.
First published June 27, 2008; doi:10.1152/ajpheart.00023.2008.

Muscle mechanoreflex augments arterial baroreflex-mediated dynamic sympathetic response to carotid sinus pressure

Kenta Yamamoto,[1,2] Toru Kawada,[2] Atsunori Kamiya,[2] Hiroshi Takaki,[2] Toshiaki Shishido,[2] Kenji Sunagawa,[3] and Masaru Sugimachi[2]

[1]*Consolidated Research Institute for Advanced Science and Medical Care, Waseda University, Tokyo;* [2]*Department of Cardiovascular Dynamics, Advanced Medical Engineering Center, National Cardiovascular Center Research Institute, Osaka; and* [3]*Department of Cardiovascular Medicine, Graduate School of Medical Sciences, Kyushu University, Fukuoka, Japan*

Submitted 8 January 2008; accepted in final form 19 June 2008

Yamamoto K, Kawada T, Kamiya A, Takaki H, Shishido T, Sunagawa K, Sugimachi M. Muscle mechanoreflex augments arterial baroreflex-mediated dynamic sympathetic response to carotid sinus pressure. *Am J Physiol Heart Circ Physiol* 295: H1081–H1089, 2008. First published June 27, 2008; doi:10.1152/ajpheart.00023.2008.—Although the muscle mechanoreflex is one of the pressor reflexes during exercise, its interaction with dynamic characteristics of the arterial baroreflex remains to be quantitatively analyzed. In anesthetized, vagotomized, and aortic-denervated rabbits ($n = 7$), we randomly perturbed isolated carotid sinus pressure (CSP) using binary white noise while recording renal sympathetic nerve activity (SNA) and arterial pressure (AP). We estimated the transfer functions of the baroreflex neural arc (CSP to SNA) and peripheral arc (SNA to AP) under conditions of control and muscle stretch of the hindlimb (5 kg of tension). The muscle stretch increased the dynamic gain of the neural arc while maintaining the derivative characteristics [gain at 0.01 Hz: 1.0 ± 0.2 vs. 1.4 ± 0.6 arbitrary units (au)/mmHg, gain at 1 Hz: 1.7 ± 0.6 vs. 2.7 ± 1.4 au/mmHg; $P < 0.05$, control vs. stretch]. In contrast, muscle stretch did not affect the peripheral arc. In the time domain, muscle stretch augmented the steady-state response at 50 s (−1.1 ± 0.3 vs. −1.7 ± 0.7 au; $P < 0.05$, control vs. stretch) and negative peak response (−2.1 ± 0.5 vs. −3.1 ± 1.5 au; $P < 0.05$, control vs. stretch) in the SNA step response. A simulation experiment using the results indicated that the muscle mechanoreflex would accelerate the closed-loop AP regulation via the arterial baroreflex.

muscle stretch; transfer function; exercise pressor reflex; exercise; arterial pressure

THE ARTERIAL BAROREFLEX SYSTEM plays an important role in stabilizing arterial pressure (AP) during daily activity. Knowledge of the open-loop static and dynamic characteristics of the arterial baroreflex is essential for a systematic understanding of how the baroreflex system regulates AP. The static characteristics provide information on the operating point of the baroreflex system (19, 34, 48), whereas the dynamic characteristics determine the stability and quickness of the baroreflex system (14, 22, 23). Importantly, many previous studies showed that exercise resets the baroreflex function (3, 5, 6, 29, 30, 32, 35, 36, 40, 45, 47). However, only a few investigations focused on the dynamic characteristics of the arterial baroreflex during exercise (10, 36, 38, 57). The dynamic characteristics of the arterial baroreflex determine how quickly or slowly the system would response to baroreceptor pressure perturbations. Such information cannot be obtained from the static characteristics alone.

The neural mechanisms responsible for changes in the baroreflex function during exercise are considered to be mediated by central command (6, 13, 29, 39, 46) and by afferent inputs from metabolic and mechanical-sensitive skeletal muscle receptors (11, 12, 17, 41, 43, 44, 49). Regarding the static interaction between the muscle mechanoreflex and arterial baroreflex, we performed a baroreflex open-loop study and reported that muscle stretch extended the response range of sympathetic nerve activity (SNA) to baroreceptor pressure input (58, 59). Based on the results, we hypothesized that the activation of the muscle mechanoreflex would augment the dynamic SNA response to baroreceptor pressure input under open-loop conditions. To the best of our knowledge, however, the effects of the muscle mechanoreflex on the dynamic characteristics of the arterial baroreflex have never been reported.

To test the above hypothesis, we identified the dynamic characteristics of the baroreflex during muscle stretch in anesthetized rabbits under baroreflex open-loop conditions (14, 22, 23). The transfer functions from baroreceptor pressure input to SNA (the baroreflex neural arc) and from SNA to AP (the baroreflex peripheral arc) were estimated by a white noise approach (51). The "whiteness" is essential for the system identification of the arterial baroreflex because it is equivalent mathematically to test the system with all possible pressure changes within the frequency range of interest.

METHODS

Surgical preparations. Animals were cared for in strict accordance with the Guiding Principles for the Care and Use of Animals in the Field of Physiological Sciences approved by the Physiological Society of Japan. All protocols were approved by the Animal Subjects Committee of the National Cardiovascular Center. Seven Japanese White rabbits weighing 2.6–3.0 kg were anesthetized via an intravenous injection (2 ml/kg) of a mixture of urethane (250 mg/ml) and α-chloralose (40 mg/ml) and were mechanically ventilated with oxygen-enriched room air. Supplemental anesthetics (0.2–0.3 $ml \cdot kg^{-1} \cdot h^{-1}$) were administered continuously to maintain stable AP and heart rate levels during intervals of experimental protocols, which were indicative of an appropriate level of anesthesia. Arterial blood was sampled from the left common carotid artery. Rabbits were slightly hyperventilated to suppress chemoreflexes (arterial P_{CO_2} ranged from 30 to 35 mmHg, arterial $P_{O_2} > 300$ mmHg). Arterial blood pH was within the

Address for reprint requests and other correspondence: K. Yamamoto, Consolidated Research Institute for Advanced Science and Medical Care, Waseda Univ., 513 Wasedatsurumakicho, Shinjuku, Tokyo 162-0041, Japan (e-mail: kenta@aoni.waseda.jp).

The costs of publication of this article were defrayed in part by the payment of page charges. The article must therefore be hereby marked "*advertisement*" in accordance with 18 U.S.C. Section 1734 solely to indicate this fact.

physiological range when examined at the end of the surgical preparation as well as at the end of the experiment. The body temperature of each animal was maintained at ~38°C with a heating pad. AP was measured using a high-fidelity pressure transducer (Millar Instruments, Houston, TX) inserted from the right femoral artery to the aortic arch.

We isolated bilateral carotid sinuses from the systemic circulation by ligating the internal and external carotid arteries and other small branches originating from the carotid sinus region. Isolated carotid sinuses were filled with warmed physiological saline via catheters inserted through the common carotid arteries. Intra-CSP was controlled by a servo-controlled piston pump (model ET-126A, Labworks, Costa Mesa, CA). Bilateral vagal and aortic depressor nerves were sectioned at the neck to minimize reflexes from the cardiopulmonary region and from the aortic arch.

We exposed the left renal sympathetic nerve retroperitoneally and attached a pair of stainless steel wire electrodes (Bioflex wire AS633, Cooner Wire, Chatsworth, CA) to record SNA. The nerve bundle peripheral to the electrodes was tightly ligated and crushed to eliminate afferent signals from the kidney. The nerve and electrodes were secured with silicone glue (Kwik-Sil, World Precision Instruments, Sarasota, FL). The preamplified nerve signal was band-pass filtered at 150–1,000 Hz, full-wave rectified, and low-pass filtered with a cutoff frequency of 30 Hz to quantify the nerve activity.

With the rabbit in the prone position, the sacrum, left ankle, and knee were clamped with a custom-made apparatus to prevent body trunk and hindlimb movement during muscle stretch. The left triceps surae muscle, Achilles tendon, and calcaneus bone were exposed. The left triceps surae muscle was isolated from the surrounding tissue. The Achilles tendon was severed from the calcaneus bone and attached to a force transducer (Load Cell LUR-A-SA1, Kyowa Electronic Instruments, Tokyo, Japan). During muscle stretch, the other side of the force transducer was connected to a 5-kg weight via a pulley.

Protocols. To obtain operating pressure values, the carotid sinus baroreflex negative feedback loop was effectively closed by adjusting CSP to AP. Mean AP (and thus mean CSP) at steady state was treated as the operating pressure under control conditions. We then performed muscle stretch for 1 min while the carotid sinus baroreflex was effectively closed. Mean AP during the last 10 s of muscle stretch was treated as the operating pressure under muscle stretch conditions.

To estimate the baroreflex dynamic characteristics, CSP was assigned either high (+20 mmHg) or low (−20 mmHg) pressure values around the operating pressure according to a binary white noise sequence. The switching interval of the binary white noise signal was set at 500 ms so that the CSP power spectrum was fairly flat up to 1 Hz. We confirmed that the muscle stretch produced a sustained SNA increase for at least 7 min (58). To limit the maximum duration of muscle stretch within this time period, a 6-min CSP perturbation was performed twice using different binary sequences, and the two sets of data were pooled for analyses under both control and muscle stretch conditions. The order of control and muscle stretch conditions was randomized across the animals.

Data analysis. We recorded CSP, muscle tension, SNA, and AP at a sampling rate of 200 Hz using a 12-bit analog-to-digital converter. Data were stored on a dedicated laboratory computer system.

To estimate the neural arc transfer function of the carotid sinus baroreflex, we treated CSP as the input and SNA as the output of the system. In the peripheral arc transfer function, we treated SNA as the input and AP as the output of the system. In the total loop transfer function, we treated CSP as the input and AP as the output of the system. Data analysis was started from 90 s after the initiation of each trial to process the stationary portion of data without the effects of transition from closed-loop CSP waveform to open-loop binary white noise CSP input and the transition from nonstretch to stretch of muscle mechanoreceptors. The input-output data pairs were resampled at 10 Hz and segmented into 50%-overlapping bins of 1,024 points each. For each segment, a linear trend was subtracted, and a Hanning window was applied. A fast Fourier transform was performed to obtain the frequency spectra of the input and output signals. The ensemble averages of input power spectral density [$S_{XX}(f)$], output power spectral density [$S_{YY}(f)$], and cross-spectral density between the input and output [$S_{YX}(f)$] were obtained over eight segments derived from two sets of data, where f represents frequency. Finally, we calculated the transfer function from input to output [$H(f)$] using the following equation (27):

$$H(f) = \frac{S_{YX}(f)}{S_{XX}(f)} \quad (1)$$

Hereinafter, we denote the modulus as the dynamic gain of the transfer function. To quantify the linear dependence between input and output signals in the frequency domain, we calculated a magnitude-squared coherence function [Coh(f)] using the following equation (27):

$$\mathrm{Coh}(f) = \frac{|S_{YX}(f)|^2}{S_{XX}(f)S_{YY}(f)} \quad (2)$$

The coherence value ranges from zero to unity. Unity coherence indicates perfect linear dependence between input and output signals, whereas zero coherence indicates total independence between the two signals.

To facilitate an intuitive understanding of the transfer function, the step response corresponding to the transfer function was also calculated as follows. The system impulse response was derived from the inverse Fourier transform of $H(f)$. The step response was obtained from the time integral of the impulse response.

Statistical analysis. All data are presented as means ± SD. Because the amplitude of SNA varied depending on recording conditions, such as the physical contact between the nerve and electrodes, SNA was presented in arbitrary units (au). Neural and peripheral arc transfer functions were normalized in each animal so that the average gain values below 0.03 Hz in the control trial became unity. To compare the transfer functions between two conditions, a transfer gain value at 0.01 Hz ($G_{0.01}$), 0.1 Hz ($G_{0.1}$), 0.5 Hz ($G_{0.5}$), and 1 Hz (G_1) were calculated. In the step response of the neural arc, the steady-state step response at 50 s (S_{50}), the negative peak value (S_{peak}), and the time to negative peak (T_{peak}) were calculated. The effects of muscle stretch on these parameters were examined using the paired t-test. Differences were considered significant when $P < 0.05$.

RESULTS

Figure 1 shows a typical time series of CSP, muscle tension, SNA, and AP under control (*left*) and muscle stretch (*right*) conditions. Although the same binary sequence was applied for two conditions in each animal, different binary sequences were applied for different animals to reduce possible systematic errors in system identification caused by a bias in whiteness specific to a selected binary sequence. The mean CSP during muscle stretch conditions (Fig. 1, *right*) was set higher than that during the control conditions (Fig. 1, *left*) to mimic the increase in the operating pressure during muscle stretch under baroreflex closed-loop conditions (i.e., the AP increase by muscle stretch increases the mean input pressure to the baroreceptors) . Muscle stretch increased mean levels of SNA and AP compared with control conditions during the experiment (Table 1).

Figure 2 shows the transfer functions of the neural (*left*) and peripheral (*right*) arcs estimated under the control and muscle stretch conditions; gain plots (*top*), phase plots (*middle*), and Coh(f) (*bottom*) are also presented. The thin and thick solid lines in Fig. 2 indicate control and muscle stretch conditions, respectively. In the neural arc, the dynamic gain increased as

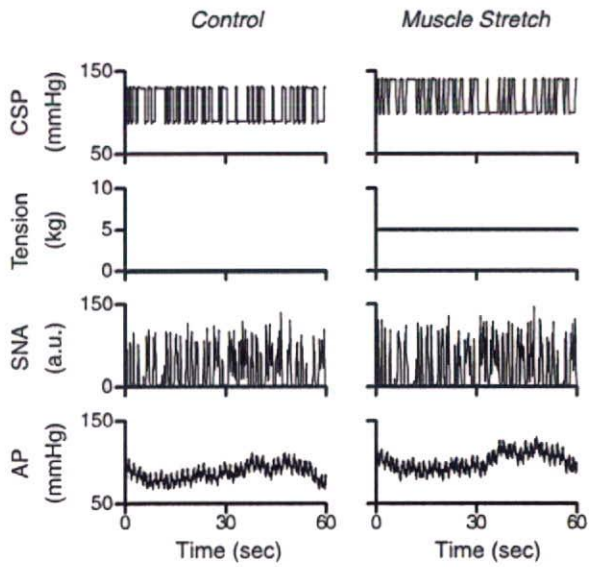

Fig. 1. Typical time series of intracarotid sinus pressure (CSP), muscle tension, sympathetic nerve activity [SNA; in arbitrary units (au)], and arterial pressure (AP) under control (*left*) and muscle stretch (*right*) conditions. CSP was perturbed according to a binary white noise sequence. Muscle stretch increased mean levels of SNA and AP under muscle stretch conditions compared with the control conditions.

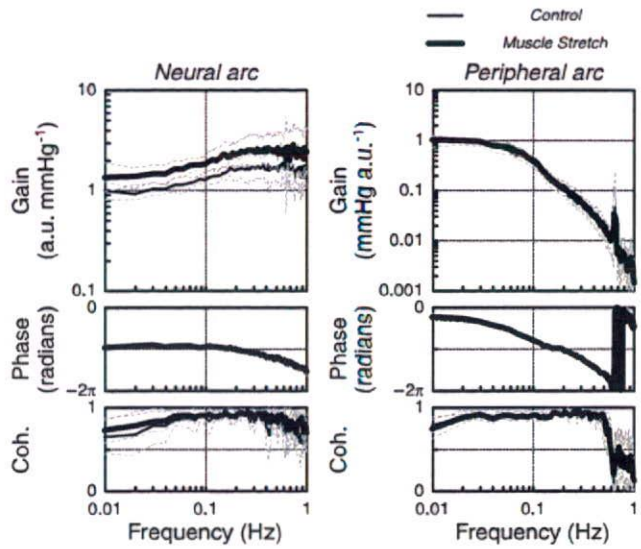

Fig. 2. Transfer functions of the neural (*left*) and peripheral (*right*) arcs under control and muscle stretch conditions. In the neural arc, the input was CSP and the output was SNA. In the peripheral arc, the input was SNA and the output was AP. The mean level of CSP input to the neural arc was set higher under muscle stretch conditions than under control conditions to mimic the physiological condition (i.e., baroreflex closed-loop conditions). Gain plots (*top*), phase plots (*middle*) and coherence (Coh) functions (*bottom*) are shown. Thin and thick solid lines indicate control and muscle stretch conditions, respectively. In the neural arc (*left*), muscle stretch caused an approximately parallel upward shift of the gain plot. Solid and dashed lines represent means and means ± SD values, respectively.

the frequency of input modulation increased under both conditions, indicating derivative characteristics of the neural arc. Muscle stretch caused an approximately parallel upward shift of the gain plot. The phase approached $-\pi$ radians ($-180°$) at the lowest frequency (0.01 Hz) under both conditions, reflecting the negative feedback character of the baroreflex neural arc (i.e., an increase in CSP decreased SNA). Phase plots were nearly superimposed between the two conditions. Coherence values did not differ between both conditions. In the peripheral arc, the dynamic gain decreased in the frequency range from 0.05 to 1 Hz as the frequency of input modulation increased under both conditions, indicating the low-pass characteristics of the peripheral arc. The phase approached 0 radians at the lowest frequency (0.01 Hz) under both conditions, reflecting the fact that an increase in SNA increased AP. The phase lagged with increasing frequency up to 1 Hz. The gain plot, phase plot, and Coh(f) did not differ between both conditions.

Table 2 summarizes gains of the transfer functions. In the neural arc, $G_{0.01}$, $G_{0.1}$, $G_{0.5}$, and G_1 were higher under muscle

Table 1. *Mean levels and CVs of CSP, SNA, and AP at 1, 2, 4, and 6 min under control and muscle stretch conditions*

	Time			
	1 min	2 min	4 min	6 min
		CSP		
Control	95±18	96±18	95±18	96±18
CV	13±2	12±3	11±3	14±2
Muscle stretch	114±15*	115±16*	113±16*	114±15*
CV	11±2	11±1	10±2	12±2
		SNA		
Control	102±4	99±5	100±4	99±4
CV	46±11	45±9	43±9	47±9
Muscle stretch	133±22*	129±21*	127±17*	126±17*
CV	48±11	47±8	44±9	49±10
		AP		
Control	90±21	89±20	88±16	88±18
CV	7±2	6±2	6±2	6±2
Muscle stretch	107±26*	105±22*	104±15*	101±15*
CV	7±3	6±3	6±3	7±2

Values are means ± SD; n = 7. CSP, carotid sinus pressure (in mmHg); SNA, sympathetic nerve activity (in %); AP, arterial pressure (in mmHg); CV, coefficient of variation. Mean and CV values were calculated from 30-s data ending at each time point. *P < 0.05 vs. control.

Table 2. *Gains of the transfer functions*

	Control	Muscle Stretch
Neural arc		
$G_{0.01}$, au/mmHg	1.01±0.23	1.44±0.56*
$G_{0.1}$, au/mmHg	1.30±0.11	1.86±0.37*
$G_{0.5}$, au/mmHg	1.77±0.64	2.65±1.08*
G_1, au/mmHg	1.72±0.66	2.72±1.40*
Peripheral arc		
$G_{0.01}$, mmHg/au	1.08±0.06	1.06±0.20
$G_{0.1}$, mmHg/au	0.37±0.09	0.42±0.09
$G_{0.5}$, mmHg/au	0.02±0.01	0.02±0.01
G_1, mmHg/au	0.004±0.001	0.004±0.002
Total loop		
$G_{0.01}$, mmHg/mmHg	1.08±0.18	1.53±0.63*
$G_{0.1}$, mmHg/mmHg	0.48±0.12	0.81±0.31*
$G_{0.5}$, mmHg/mmHg	0.04±0.04	0.06±0.04*
G_1, mmHg/mmHg	0.006±0.003	0.013±0.013

Values are means ± SD; n = 7. $G_{0.01}$, $G_{0.1}$, $G_{0.5}$, and G_1, dynamic gains at 0.01, 0.1, 0.5, and 1 Hz, respectively; au, arbitrary units. *P < 0.05 vs. control.

stretch compared with control conditions. In the peripheral arc, $G_{0.01}$, $G_{0.1}$, $G_{0.5}$, and G_1 were unchanged between control and muscle stretch conditions.

Figure 3 shows the total baroreflex loop transfer functions (CSP to AP) under control and muscle stretch conditions. The thin and thick solid lines in Fig. 3 indicate control and muscle stretch conditions, respectively. The dynamic gain decreased as the frequency of input modulation increased under both conditions, indicating low-pass characteristics. The dynamic gain under muscle stretch conditions was higher than that under control conditions in frequency from 0.01 to 0.5 Hz (Table 2). The phase plot and Coh(f) did not differ between both conditions.

Figure 4 shows step responses of SNA corresponding to the transfer functions in the neural arc shown in Fig. 2. The initial drop in the SNA response as well as the steady-state response was augmented during muscle stretch (Table 3). T_{peak} did not differ between control and muscle stretch conditions (Table 3).

DISCUSSION

The key new findings of the present study are as follows. Muscle stretch increased the dynamic gain of the carotid sinus baroreflex neural arc as estimated by binary white noise input (Fig. 2). In contrast, the peripheral arc transfer function remained unchanged irrespective of the muscle stretch (Fig. 2). These results suggest that during muscle mechanoreflex activation, the dynamic SNA response to CSP perturbation is augmented.

System identification by the white noise approach. To identify the dynamic characteristics of arterial baroreflex function quantitatively, we described the carotid sinus baroreflex control of SNA and AP in terms of system identification using the white noise technique. Compared with the traditional approach of testing dynamic properties of the physiological system with step and sine wave stimuli, the white noise approach has definite advantages, as follows (27). First, if a step stimulus is applied, we learn the response of the system to this step and have little notion of the response of the system to any other type of stimulus. If a sinusoidal pulse is applied, then we know the response of the system to such a stimulus and little else. The same applies for any other specific waveform. Theoretically speaking, the system is tested with every possible stimulus in the white noise approach. The white noise stimulus is a very rich stimulus. It should be emphasized that the white noise method is perfectly suited to the analysis of linear systems. As shown in Figs. 2 and 3, high coherence values close to unity indicate the validity of our method for system identification. Second, the identification of the physiological system through the white noise technique is largely unaffected by the types of contaminating noise usually present in such a system. Our study provides the first and quantitative description of the dynamic characteristics of the carotid sinus baroreflex during isolated activation of mechanosensitive afferents from skeletal muscle.

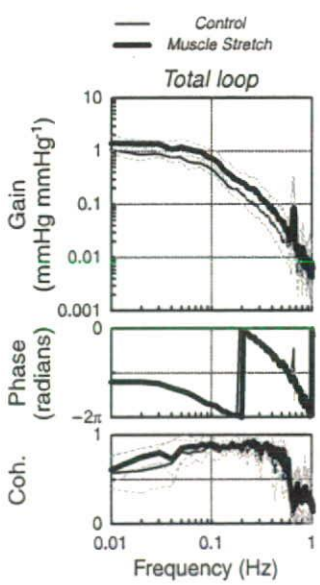

Fig. 3. Total loop transfer functions from CSP to AP under control and muscle stretch conditions. Gain plots (*top*), phase plots (*middle*) and coherence functions (*bottom*) are shown. Thin and thick solid lines indicate control and muscle stretch conditions, respectively. The dynamic gain decreased as the frequency of input modulation increased under both conditions, indicating low-pass characteristics. Muscle stretch caused an approximately parallel upward shift of the gain plot. Solid and dashed lines represent means and means ± SD values, respectively.

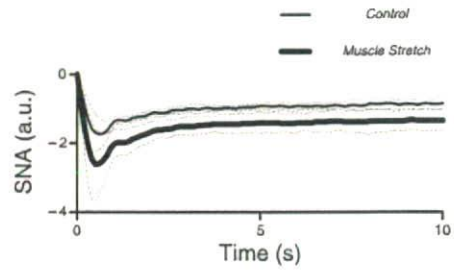

Fig. 4. Step responses corresponding to transfer functions of the neural arc obtained from Fig. 2, showing the SNA response to a 1-mmHg increase in input pressure. Thin and thick solid lines indicate control and muscle stretch conditions, respectively. The initial drop in the SNA response as well as the steady-state response was augmented by the muscle stretch. Solid and dashed lines represent means and means ± SD values, respectively.

Effects of the muscle mechanoreflex on dynamic characteristics of the carotid sinus baroreflex. The effects of activation of afferents from skeletal muscle, such as those occurring during exercise, on the arterial baroreflex have been extensively studied (5, 13, 29, 42, 43, 49, 58, 59). These studies have demonstrated that the afferent input from muscle resets the baroreflex control of AP, heart rate, and SNA. However, the dynamic characteristics of the arterial baroreflex during isolated activation of muscle mechanosensitive afferents have never been analyzed. In the present study, muscle stretch increased dynamic gain in every frequency (Fig. 2 and Table

Table 3. *Parameters of step responses*

	Control	Muscle Stretch
S_{50}, au	−1.05±0.30	−1.69±0.69*
S_{peak}, au	−2.10±0.50	−3.08±1.45*
T_{peak}, s	0.63±0.21	0.64±0.20

Values are means ± SD; n = 7. A step response is defined as a SNA response to a 1-mmHg change in input pressure. S_{50}, step response at 50 s; S_{peak}, negative peak response; T_{peak}, time to negative peak. *$P < 0.05$ vs. control.

2), whereas it did not affect the peripheral arc. These data are the first to provide quantitative evidence demonstrating that the dynamic SNA response to CSP perturbation is augmented during isolated activation of the muscle mechanoreflex. Although an increase in dynamic gain in the lowest frequency (0.01 Hz) was expected from the results of our previous studies showing an increase in static gain by muscle stretch (58, 59), the information was insufficient to perform a simulation study to examine the effects of muscle stretch on the closed-loop dynamic AP regulation (see *Physiological implications*). The present study extended our previous work by providing additional information on the dynamic interaction over a wide range of frequencies between 0.01 and 1 Hz in the carotid sinus baroreflex.

The static characteristics of the arterial baroreflex determine an operating point of the baroreflex system. Furthermore, the static characteristics described by a modeled sigmoid function provide the parameters of threshold, saturation, and maximal gain at the centering point. However, the static characteristics alone cannot provide the information on the changes over time in the response of the baroreflex system. On the other hand, dynamic analysis techniques such as transfer function analysis estimated by the white noise approach provide information on the stability and quickness of the system response. The dynamic SNA response to baroreceptor pressure input became greater as the frequency of input modulation increased, suggesting derivative characteristics (i.e., high-pass characteristics) of the baroreflex neural arc (Fig. 2, *left*, thin solid line). In contrast, the dynamic AP response to SNA became smaller as the frequency of SNA modulation increased, indicating low-pass characteristics of the baroreflex peripheral arc (Fig. 2, *right*, thin solid line). The total loop transfer function (CSP to AP) is determined by a product of the neural and peripheral arc transfer functions (Fig. 3, thin solid line). Therefore, the decreasing slope of dynamic gain in the total loop transfer function was shallower than that in the corresponding peripheral arc. In other words, the fast neural arc effectively compensates for the slow peripheral arc to accelerate dynamic AP regulation by the baroreflex negative-feedback loop (14). During muscle stretch, the dynamic gain in the neural arc was increased by ~50% in every frequency under study (Fig. 2 and Table 2), indicating that the derivative characteristics of the neural arc were maintained. As a result, the effect of the neural arc compensating for the slow AP response was preserved during the activation of muscle mechanoreflex (Fig. 3 and Table 2). Furthermore, the total loop dynamic gain was augmented during the muscle stretch due to the upward shift of the neural arc transfer function.

Because we used passive muscle stretch as the input for the muscle mechanoreflex, the physiological significance of the present results should be interpreted carefully. Several studies have examined the arterial baroreflex control of SNA during static and dynamic exercise. Static and heavy dynamic exercise resets the baroreflex control of SNA to higher SNA levels with an increase in its sensitivity (9, 11, 17, 32). On the other hand, mild to moderate dynamic exercise resets the baroreflex control of SNA without any change in its sensitivity (3, 24, 38). Because the muscle mechanoreflex is activated during mild to moderate dynamic exercise (4), our results indicate that the muscle mechanoreflex may contribute to increasing the baroreflex gain of SNA during mild to moderate dynamic exercise. In addition to differences in the measured SNA (renal vs. muscle), analytic methods of baroreflex function, modes of mechanoreflex activation, and/or species between the present study and previous studies, the cardiopulmonary baroreflex should be taken into account. Charkoudian et al. (1) demonstrated that increasing central venous pressure via head-down tilt or saline infusion attenuated the baroreflex sensitivity in the control of SNA. The activation of cardiopulmonary baroreceptors induced by increasing central venous pressure may influence the arterial baroreflex control during dynamic exercise (37). In the present study, however, the cardiopulmonary baroreflex did not operate due to bilateral vagotomy.

Previous studies (7, 25) have suggested that the muscle mechanoreflex has a dominant role in pressor reflexes during muscle contraction in anesthetized or decerebrate cats. Although we believe that the mechanoreflex is one of the pressor reflexes during exercise, the functional importance of the muscle mechanoreflex in cardiovascular regulation during exercise in conscious conditions is debatable. Matsukawa et al. (28) recently reported that blockade of the muscle mechanoreflex by gadolinium did not alter AP responses to isometric exercise in conscious cats. Moreover, they found that gadolinium significantly diminished the pressor responses to passive muscle stretch in anesthetized cats. These observations suggest that, under the experimental design, the muscle mechanoreflex would not be activated during exercise or, even if it was activated, it has no functional importance in cardiovascular responses to exercise in conscious conditions. One criticism for the study is that there is always a possibility that changes in the central command in conscious conditions had compensated for the lack of muscle mechanoreflex. Further studies are needed to better understand the role of the muscle mechanoreflex on neural cardiovascular responses during exercise.

High-pass characteristics of the baroreflex neural arc. It is likely that the dynamic characteristics of the baroreflex neural arc actually reflect the intrinsic and synaptic properties of central nervous system neurons and neural circuits that transmit baroreceptor input. However, the central baroreceptor synapses are characterized as a low-pass filter (26). The difference between high-pass characteristics of the neural arc transfer gain and low-pass characteristics of the central baroreceptor synaptic transmission could be attributable to the difference of estimated frequency ranges. Frequency-dependent depression (FFD) of synaptic transmission in the baroreflex central pathways is the phenomenon that the probability of excitatory postsynaptic potentials progressively reduces as the frequency of afferent input increases beyond 1 Hz (2, 33). Although FDD and transfer gain should be discriminated in theory, interactions between FDD and transfer gain may occur when the modulation frequency of afferent fiber stimulation approached the frequency range of FDD. Indeed, Kawada et al. (23) found high-cut characteristics of the baroreflex neural arc in the frequency range above ~1 Hz. In the present study, the transfer gain was derived from 0.01 to 1 Hz. Whether the dynamic interaction between carotid sinus baroreflex and muscle mechanoreflex exists in the frequency range beyond 1 Hz awaits further studies.

Part of the high-pass characteristics in the baroreflex neural arc is attributable to the derivative nature observed in the baroreceptor transduction from CSP input to baroreceptor afferent nerve activity (i.e., mechanoneural transduction) (21).

However, we think there exists high-pass characteristics in the transduction from baroreceptor afferent input to efferent SNA, because the magnitude of high-pass characteristics slightly differs between cardiac and renal SNAs in response to the same baroreceptor pressure perturbation (18).

In an electrical circuit, we can design a high-pass filter only from low-pass filter elements using a feedback loop (Fig. 5). Although the main forward path of the baroreflex neural arc from afferent nerve activity to efferent SNA is considered to be the nucleus tructus solitarius, caudal ventrolateral medulla, and rostral ventrolateral medulla (53), there could be feedback connections between these areas. Therefore, it is possible that synaptic connection has basically low-pass characteristics, whereas the baroreflex neural arc reveals high-pass characteristics as a neural circuit. The speculation also needs to be verified experimentally in the future.

Physiological implications. Under physiological conditions, the baroreflex is closed as a negative feedback system. In the following discussion, we will focus on the effect of the augmentation of dynamic SNA modulation in the neural arc on the closed-loop dynamic AP regulation. Figure 6*A* illustrates a simulator consisting of the linear neural arc transfer function (H_N) and linear peripheral arc transfer function (H_P) followed by the nonlinear sigmoidal components (see the APPENDIX for details). A closed-loop AP response to a stepwise pressure perturbation (−40 mmHg) with pulsatile pressure was simulated, and the result is shown in Fig. 6*B*. Muscle stretch shortened the time to 95% of steady state by ~33% from 7.2 to 4.8 s (shaded and solid arrows in Fig. 6*B*). This result suggests that, under baroreflex closed-loop conditions, the rate of recovery in AP following a pressure perturbation occurs sooner when accompanied by the muscle mechanoreflex. Increasing the quickness of the negative-feedback system can be caused by augmentation and/or acceleration of the open-loop transfer function of the system. In our baroreflex open-loop experiment, S_{50} and S_{peak} in the step responses of SNA were augmented by the muscle stretch (Fig. 4 and Table 3). On the other hand, T_{peak} did not differ between control and muscle stretch conditions (Fig. 4 and Table 3). These results suggest that the improvement in the quickness of the AP restoration via the baroreflex observed in the closed-loop simulation was induced by augmentation, rather than acceleration, of the dynamic SNA response in the neural arc. However, further experimental studies are needed to verify the simulation model.

Limitations. The present study has several limitations. First, we performed the experiment in anesthetized animals. Previous studies have suggested that any anesthetic could alter the baroreflex regulation in AP (54–56). The gain of the baroreflex is reported in the conscious state to be higher (~2-fold) than in the anesthetized state. A previous study (52) suggested that α-chloralose anesthesia could alter the dynamic characteristics of the baroreflex regulation around the frequency of 5 Hz. However, the anesthesia was convenient for the elimination of the central command. Furthermore, we compared the baroreflex gain between muscle stretch and nonstretch conditions both under anesthesia. Therefore, a reasonable interpretation would be that the increased baroreflex gain is attributable to muscle stretch in this experiment.

Second, stretching of skeletal muscle provides a stimulus for the activation of mechanoreceptors that is different from that which occurs during muscle contraction. During contraction, mechanoreceptors are activated by a shortening of skeletal muscle and by compression of the receptors. Thus, mechanoreceptors may be stimulated in a very different manner during stretch, which would likely affect the magnitude of the corresponding reflex response. In addition, the level of muscle stretch used in our experiment was relatively high (50). The stretch may activate different afferents than contraction (8). Furthermore, the discharge profile of mechanosensitive afferents adapt during static muscle stretch (31). Accordingly, during the muscle stretch for 6 min in the present study, the firing level from the mechanoreceptors might have been

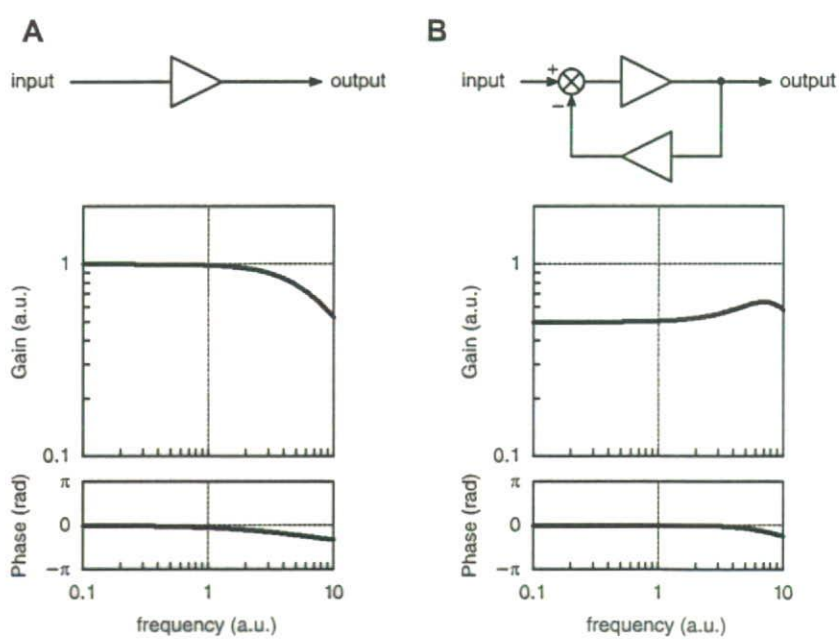

Fig. 5. An example that a circuit consisting of only low-pass elements yields high-pass characteristics as a circuit. *A*: block diagram of a single low-pass element (triangle) and its transfer function. Units for gain and frequency are arbitrary. *B*: block diagram of a circuit with a negative feedback loop with the same low-pass element (triangles). Because gain in the lower frequency range is attenuated more by the low-pass characteristics of the feedback path, the transfer function from input to output reveals high-pass characteristics.

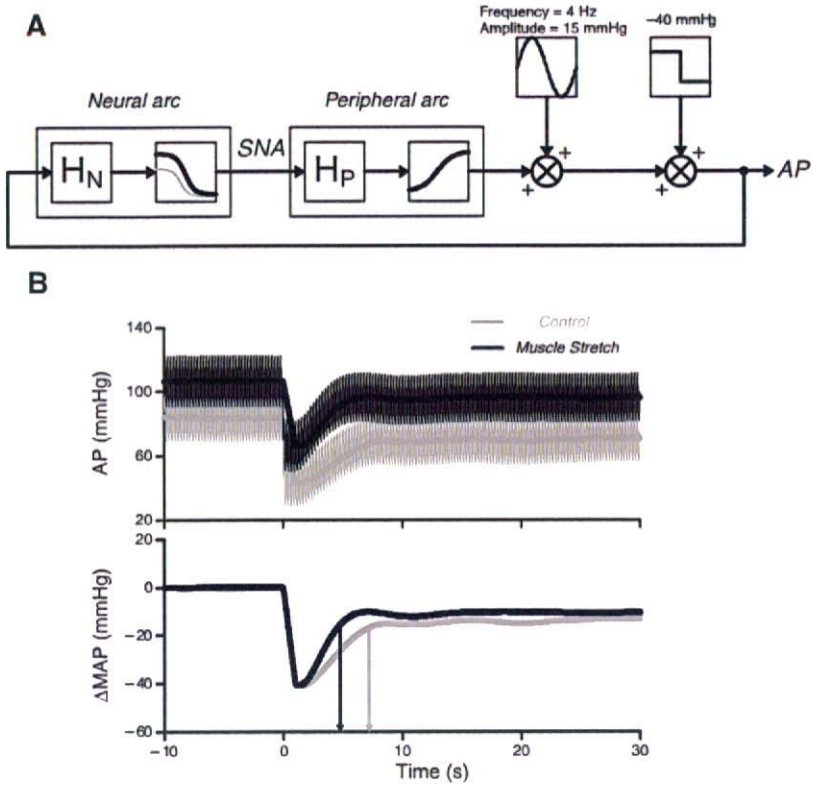

Fig. 6. *A*: simulator of the baroreflex system during activation of the muscle mechanoreflex. A stepwise perturbation with pulsatile pressure was applied to the baroreflex negative feedback system (see the APPENDIX for details). H_N, neural arc transfer function; H_P, peripheral arc transfer function. *B*: simulation results of the closed-loop AP response to the stepwise pressure perturbation (−40 mmHg). Muscle stretch shortened the time to 95% of steady state by ~33% (shaded and solid arrows). Shaded and solid thick lines indicate mean AP (MAP) resampled at 1 Hz. ΔMAP, change in MAP from baseline.

steadily diminishing. In fact, the increase in SNA and AP induced by muscle stretch gradually decreased from 90 s to 6 min after the initiation of the muscle stretch, which was used for data analysis (Table 1). However, SNA and AP remained significantly higher under muscle stretch conditions than control conditions over the protocol for 6 min. Thus, we believe that the mechanoreflex remained activated in this protocol. Further studies are required to elucidate the dynamic interactions between baroreflex and mechanoreflex induced by different modes of activation, such as cyclic activation of the mechanoreflex.

Third, the transfer function analysis is useful in identifying the linear input-output relationship of the baroreflex at a given operating point. However, the transfer function cannot characterize the nonlinear input-output relationship of the system. In the presence of nonlinear system behavior such as the baroreflex system, the transfer function analysis is partly compromised, indicating that the absolute output values of the nonlinear system to given input signals cannot be predicted accurately by the transfer function alone. Combining a linear transfer function with a nonlinear sigmoidal element would increase the accuracy to reproduce dynamic characteristics observed in the baroreflex neural arc (20, 22).

Finally, we measured renal SNA as a proxy of systemic sympathetic activity. SNAs to different organs may vary a lot. Although static and dynamic regulations of the baroreflex neural arc are similar among renal, cardiac, and muscle SNAs (15, 16, 18), whether this holds true during muscle stretch remains to be verified. Also, subsystems of the peripheral arc transfer function such as those relating cardiac output and peripheral vascular resistance remain to be identified.

Conclusions. In conclusion, baroreflex open-loop transfer function analysis demonstrated that the activation of mechanosensitive afferents from skeletal muscles augmented the dynamic SNA response in the neural arc. This augmentation of the dynamic SNA response with maintained derivative characteristics of the neural arc may accelerate closed-loop AP regulation via the baroreflex.

APPENDIX

To simulate the closed-loop AP response to stepwise pressure perturbation (Fig. 6), we used the derivative-sigmoidal cascade model. The cascade model consists of a linear derivative filter followed by a nonlinear sigmoidal component (20, 22).

We modeled the sigmoidal nonlinearity in the baroreflex neural arc interacting with the muscle mechanoreflex by the following four-parameter logistic function with threshold according to a previous study (59):

$$y = \max\left\{\frac{P_1}{1 + \exp[P_2(x - P_3)]} + P_4,\ \mathrm{Th}\right\} \qquad (A1)$$

where x and y are input (in mmHg) and output (in au) values. P_1 denotes the response range (in au), P_2 is the coefficient of gain, P_3 is the midpoint of the input range (in mmHg), P_4 is the minimum output value of the symmetric sigmoid curve (in au), and Th is a threshold value for the output (in au). The function $\max\{a,b\}$ gives the greater or equal value between a and b. We set $P_1 = 135$ au, $P_2 = 0.13$, $P_3 = 110$ mmHg, $P_4 = -40$ au, and Th = 0 au. Under muscle stretch conditions, the value of P_4 was changed to 5 au. These settings were determined based on the static interaction

between the baroreflex and muscle mechanoreflex obtained from previous studies (58, 59).

The sigmoidal nonlinearity in the peripheral arc was modelled by a four-parameter logistic function as follows:

$$z = \frac{Q_1}{1 + \exp[Q_2(y - Q_3)]} + Q_4 \qquad (A2)$$

where y and z are input (in au) and output (in mmHg) values. Q_1 denotes the response range (in mmHg), Q_2 is the coefficient of gain, Q_3 is the midpoint of the input range (in au), and Q_4 is the minimum output value (in mmHg). We set $Q_1 = 120$ mmHg, $Q_2 = -0.05$, $Q_3 = 70$ au, and $Q_4 = 30$ mmHg under both conditions, according to a previous study (58).

The neural arc (H_N) and peripheral arc (H_P) linear transfer functions under control and muscle stretch conditions were obtained from Fig. 2. Because absolute values of the steady-state gains in the neural and peripheral arcs were determined by a sigmoid curve (*Eqs. A1* and *A2*), the steady-state gains of H_N and H_P under both conditions were normalized to unity.

The input amplitude of the stepwise pressure perturbation was −40 mmHg. To mimic pulsatile pressure, we imposed a sinusoidal input on the output from the peripheral arc. The frequency and zero to peak amplitude of the sinusoidal input were 4 Hz and 15 mmHg, respectively (Fig. 6*A*). The closed-loop AP response was simulated up to 30 s (Fig. 6*B*).

GRANTS

This work was supported by Ministry of Health, Labour and Welfare of Japan Health and Labour Sciences Research Grant for Research on Advanced Medical Technology, Health and Labour Sciences Research Grant for Research on Medical Devices for Analyzing, Supporting and Substituting the Function of Human Body, and Health and Labour Sciences Research Grants H18-Iryo-Ippan-023 and H18-Nano-Ippan-003; the Industrial Technology Research Grant Program of the New Energy and Industrial Technology Development Organization of Japan; and Ministry of Education, Culture, Sports, Science and Technology Grant-In-Aid for Scientific Research 18591992.

REFERENCES

1. **Charkoudian N, Martin EA, Dinenno FA, Eisenach JH, Dietz NM, Joyner MJ.** Influence of increased central venous pressure on baroreflex control of sympathetic activity in humans. *Am J Physiol Heart Circ Physiol* 287: H1658–H1662, 2004.
2. **Chen CY, Horowitz JM, Bonham AC.** A presynaptic mechanism contributes to depression of autonomic signal transmission in NTS. *Am J Physiol Heart Circ Physiol* 277: H1350–H1360, 1999.
3. **Fadel PJ, Ogoh S, Watenpaugh DE, Wasmund W, Olivencia-Yurvati A, Smith ML, Raven PB.** Carotid baroreflex regulation of sympathetic nerve activity during dynamic exercise in humans. *Am J Physiol Heart Circ Physiol* 280: H1383–H1390, 2001.
4. **Gallagher KM, Fadel PJ, Smith SA, Norton KH, Querry RG, Olivencia-Yurvati A, Raven PB.** Increases in intramuscular pressure raise arterial blood pressure during dynamic exercise. *J Appl Physiol* 91: 2351–2358, 2001.
5. **Gallagher KM, Fadel PJ, Stromstad M, Ide K, Smith SA, Querry RG, Raven PB, Secher NH.** Effects of exercise pressor reflex activation on carotid baroreflex function during exercise in humans. *J Physiol* 533: 871–880, 2001.
6. **Gallagher KM, Fadel PJ, Stromstad M, Ide K, Smith SA, Querry RG, Raven PB, Secher NH.** Effects of partial neuromuscular blockade on carotid baroreflex function during exercise in humans. *J Physiol* 533: 861–870, 2001.
7. **Hayes SG, Kaufman MP.** Gadolinium attenuates exercise pressor reflex in cats. *Am J Physiol Heart Circ Physiol* 280: H2153–H2161, 2001.
8. **Hayes SG, Kindig AE, Kaufman MP.** Comparison between the effect of static contraction and tendon stretch on the discharge of group III and IV muscle afferents. *J Appl Physiol* 99: 1891–1896, 2005.
9. **Ichinose M, Saito M, Fujii N, Ogawa T, Hayashi K, Kondo N, Nishiyasu T.** Modulation of the control of muscle sympathetic nerve activity during incremental leg cycling. *J Physiol* 586: 2753–2766, 2008.
10. **Ichinose M, Saito M, Kondo N, Nishiyasu T.** Time-dependent modulation of arterial baroreflex control of muscle sympathetic nerve activity during isometric exercise in humans. *Am J Physiol Heart Circ Physiol* 290: H1419–H1426, 2006.
11. **Ichinose M, Saito M, Wada H, Kitano A, Kondo N, Nishiyasu T.** Modulation of arterial baroreflex control of muscle sympathetic nerve activity by muscle metaboreflex in humans. *Am J Physiol Heart Circ Physiol* 286: H701–H707, 2004.
12. **Ichinose M, Saito M, Wada H, Kitano A, Kondo N, Nishiyasu T.** Modulation of arterial baroreflex dynamic response during muscle metaboreflex activation in humans. *J Physiol* 544: 939–948, 2002.
13. **Iellamo F, Legramante JM, Raimondi G, Peruzzi G.** Baroreflex control of sinus node during dynamic exercise in humans: effects of central command and muscle reflexes. *Am J Physiol Heart Circ Physiol* 272: H1157–H1164, 1997.
14. **Ikeda Y, Kawada T, Sugimachi M, Kawaguchi O, Shishido T, Sato T, Miyano H, Matsuura W, Alexander J Jr, Sunagawa K.** Neural arc of baroreflex optimizes dynamic pressure regulation in achieving both stability and quickness. *Am J Physiol Heart Circ Physiol* 271: H882–H890, 1996.
15. **Kamiya A, Kawada T, Yamamoto K, Michikami D, Ariumi H, Miyamoto T, Shimizu S, Uemura K, Aiba T, Sunagawa K, Sugimachi M.** Dynamic and static baroreflex control of muscle sympathetic nerve activity (SNA) parallels that of renal and cardiac SNA during physiological change in pressure. *Am J Physiol Heart Circ Physiol* 289: H2641–H2648, 2005.
16. **Kamiya A, Kawada T, Yamamoto K, Michikami D, Ariumi H, Miyamoto T, Uemura K, Sugimachi M, Sunagawa K.** Muscle sympathetic nerve activity averaged over 1 minute parallels renal and cardiac sympathetic nerve activity in response to a forced baroreceptor pressure change. *Circulation* 112: 384–386, 2005.
17. **Kamiya A, Michikami D, Fu Q, Niimi Y, Iwase S, Mano T, Suzumura A.** Static handgrip exercise modifies arterial baroreflex control of vascular sympathetic outflow in humans. *Am J Physiol Regul Integr Comp Physiol* 281: R1134–R1139, 2001.
18. **Kawada T, Shishido T, Inagaki M, Tatewaki T, Zheng C, Yanagiya Y, Sugimachi M, Sunagawa K.** Differential dynamic baroreflex regulation of cardiac and renal sympathetic nerve activities. *Am J Physiol Heart Circ Physiol* 280: H1581–H1590, 2001.
19. **Kawada T, Shishido T, Inagaki M, Zheng C, Yanagiya Y, Uemura K, Sugimachi M, Sunagawa K.** Estimation of baroreflex gain using a baroreflex equilibrium diagram. *Jpn J Physiol* 52: 21–29, 2002.
20. **Kawada T, Uemura K, Kashihara K, Kamiya A, Sugimachi M, Sunagawa K.** A derivative-sigmoidal model reproduces operating point-dependent baroreflex neural arc transfer characteristics. *Am J Physiol Heart Circ Physiol* 286: H2272–H2279, 2004.
21. **Kawada T, Yamamoto K, Kamiya A, Ariumi H, Michikami D, Shishido T, Sunagawa K, Sugimachi M.** Dynamic characteristics of carotid sinus pressure-nerve activity transduction in rabbits. *Jpn J Physiol* 55: 157–163, 2005.
22. **Kawada T, Yanagiya Y, Uemura K, Miyamoto T, Zheng C, Li M, Sugimachi M, Sunagawa K.** Input-size dependence of the baroreflex neural arc transfer characteristics. *Am J Physiol Heart Circ Physiol* 284: H404–H415, 2003.
23. **Kawada T, Zheng C, Yanagiya Y, Uemura K, Miyamoto T, Inagaki M, Shishido T, Sugimachi M, Sunagawa K.** High-cut characteristics of the baroreflex neural arc preserve baroreflex gain against pulsatile pressure. *Am J Physiol Heart Circ Physiol* 282: H1149–H1156, 2002.
24. **Keller DM, Fadel PJ, Ogoh S, Brothers RM, Hawkins M, Olivencia-Yurvati A, Raven PB.** Carotid baroreflex control of leg vasculature in exercising and non-exercising skeletal muscle in humans. *J Physiol* 561: 283–293, 2004.
25. **Leshnower BG, Potts JT, Garry MG, Mitchell JH.** Reflex cardiovascular responses evoked by selective activation of skeletal muscle ergoreceptors. *J Appl Physiol* 90: 308–316, 2001.
26. **Liu Z, Chen CY, Bonham AC.** Frequency limits on aortic baroreceptor input to nucleus tractus solitarii. *Am J Physiol Heart Circ Physiol* 278: H577–H585, 2000.
27. **Marmarelis PZ, Marmarelis VZ.** The white noise method in system identification. In: *Analysis of Physiological Systems*. New York: Plenum, 1978, p. 131–221.
28. **Matsukawa K, Nakamoto T, Inomoto A.** Gadolinium does not blunt the cardiovascular responses at the onset of voluntary static exercise in cats: a predominant role of central command. *Am J Physiol Heart Circ Physiol* 292: H121–H129, 2007.

29. **McIlveen SA, Hayes SG, Kaufman MP.** Both central command and exercise pressor reflex reset carotid sinus baroreflex. *Am J Physiol Heart Circ Physiol* 280: H1454–H1463, 2001.
30. **Melcher A, Donald DE.** Maintained ability of carotid baroreflex to regulate arterial pressure during exercise. *Am J Physiol Heart Circ Physiol* 241: H838–H849, 1981.
31. **Mense S, Stahnke M.** Responses in muscle afferent fibres of slow conduction velocity to contractions and ischaemia in the cat. *J Physiol* 342: 383–397, 1983.
32. **Miki K, Yoshimoto M, Tanimizu M.** Acute shifts of baroreflex control of renal sympathetic nerve activity induced by treadmill exercise in rats. *J Physiol* 548: 313–322, 2003.
33. **Miles R.** Frequency dependence of synaptic transmission in nucleus of the solitary tract in vitro. *J Neurophysiol* 55: 1076–1090, 1986.
34. **Mohrman DE, Heller LJ.** Regulation of arterial pressure. In: *Cardiovascular Physiology* (4th ed.). New York: McGraw-Hill, 1997, p. 158–230.
35. **Norton KH, Boushel R, Strange S, Saltin B, Raven PB.** Resetting of the carotid arterial baroreflex during dynamic exercise in humans. *J Appl Physiol* 87: 332–338, 1999.
36. **Ogoh S, Fisher JP, Dawson EA, White MJ, Secher NH, Raven PB.** Autonomic nervous system influence on arterial baroreflex control of heart rate during exercise in humans. *J Physiol* 566: 599–611, 2005.
37. **Ogoh S, Fisher JP, Fadel PJ, Raven PB.** Increases in central blood volume modulate carotid baroreflex resetting during dynamic exercise in humans. *J Physiol* 581: 405–418, 2007.
38. **Ogoh S, Fisher JP, Raven PB, Fadel PJ.** Arterial baroreflex control of muscle sympathetic nerve activity in the transition from rest to steady-state dynamic exercise in humans. *Am J Physiol Heart Circ Physiol* 293: H2202–H2209, 2007.
39. **Ogoh S, Wasmund WL, Keller DM, AOY, Gallagher KM, Mitchell JH, Raven PB.** Role of central command in carotid baroreflex resetting in humans during static exercise. *J Physiol* 543: 349–364, 2002.
40. **Papelier Y, Escourrou P, Gauthier JP, Rowell LB.** Carotid baroreflex control of blood pressure and heart rate in men during dynamic exercise. *J Appl Physiol* 77: 502–506, 1994.
41. **Papelier Y, Escourrou P, Helloco F, Rowell LB.** Muscle chemoreflex alters carotid sinus baroreflex response in humans. *J Appl Physiol* 82: 577–583, 1997.
42. **Potts JT, Hand GA, Li J, Mitchell JH.** Central interaction between carotid baroreceptors and skeletal muscle receptors inhibits sympathoexcitation. *J Appl Physiol* 84: 1158–1165, 1998.
43. **Potts JT, Li J.** Interaction between carotid baroreflex and exercise pressor reflex depends on baroreceptor afferent input. *Am J Physiol Heart Circ Physiol* 274: H1841–H1847, 1998.
44. **Potts JT, Mitchell JH.** Rapid resetting of carotid baroreceptor reflex by afferent input from skeletal muscle receptors. *Am J Physiol Heart Circ Physiol* 275: H2000–H2008, 1998.
45. **Potts JT, Shi XR, Raven PB.** Carotid baroreflex responsiveness during dynamic exercise in humans. *Am J Physiol Heart Circ Physiol* 265: H1928–H1938, 1993.
46. **Querry RG, Smith SA, Stromstad M, Ide K, Raven PB, Secher NH.** Neural blockade during exercise augments central command's contribution to carotid baroreflex resetting. *Am J Physiol Heart Circ Physiol* 280: H1635–H1644, 2001.
47. **Rowell LB, O'Leary DS.** Reflex control of the circulation during exercise: chemoreflexes and mechanoreflexes. *J Appl Physiol* 69: 407–418, 1990.
48. **Sato T, Kawada T, Inagaki M, Shishido T, Takaki H, Sugimachi M, Sunagawa K.** New analytic framework for understanding sympathetic baroreflex control of arterial pressure. *Am J Physiol Heart Circ Physiol* 276: H2251–H2261, 1999.
49. **Smith SA, Querry RG, Fadel PJ, Gallagher KM, Stromstad M, Ide K, Raven PB, Secher NH.** Partial blockade of skeletal muscle somatosensory afferents attenuates baroreflex resetting during exercise in humans. *J Physiol* 551: 1013–1021, 2003.
50. **Stebbins CL, Brown B, Levin D, Longhurst JC.** Reflex effect of skeletal muscle mechanoreceptor stimulation on the cardiovascular system. *J Appl Physiol* 65: 1539–1547, 1988.
51. **Sugimachi M, Imaizumi T, Sunagawa K, Hirooka Y, Todaka K, Takeshita A, Nakamura M.** A new method to identify dynamic transduction properties of aortic baroreceptors. *Am J Physiol Heart Circ Physiol* 258: H887–H895, 1990.
52. **Suzuki S, Ando S, Imaizumi T, Takeshita A.** Effects of anesthesia on sympathetic nerve rhythm: power spectral analysis. *J Auton Nerv Syst* 43: 51–58, 1993.
53. **Terui N, Masuda N, Saeki Y, Kumada M.** Activity of barosensitive neurons in the caudal ventrolateral medulla that send axonal projections to the rostral ventrolateral medulla in rabbits. *Neurosci Lett* 118: 211–214, 1990.
54. **Vatner SF, Braunwald E.** Cardiovascular control mechanisms in the conscious state. *N Engl J Med* 293: 970–976, 1975.
55. **Vatner SF, Franklin D, Braunwald E.** Effects of anesthesia and sleep on circulatory response to carotid sinus nerve stimulation. *Am J Physiol* 220: 1249–1255, 1971.
56. **Vatner SF, Franklin D, Van Citters RL, Braunwald E.** Effects of carotid sinus nerve stimulation on blood-flow distribution in conscious dogs at rest and during exercise. *Circ Res* 27: 495–503, 1970.
57. **Wray DW, Fadel PJ, Keller DM, Ogoh S, Sander M, Raven PB, Smith ML.** Dynamic carotid baroreflex control of the peripheral circulation during exercise in humans. *J Physiol* 559: 675–684, 2004.
58. **Yamamoto K, Kawada T, Kamiya A, Takaki H, Miyamoto T, Sugimachi M, Sunagawa K.** Muscle mechanoreflex induces the pressor response by resetting the arterial baroreflex neural arc. *Am J Physiol Heart Circ Physiol* 286: H1382–H1388, 2004.
59. **Yamamoto K, Kawada T, Kamiya A, Takaki H, Sugimachi M, Sunagawa K.** Static interaction between muscle mechanoreflex and arterial baroreflex in determining efferent sympathetic nerve activity. *Am J Physiol Heart Circ Physiol* 289: H1604–H1609, 2005.

Vascular Endothelial Growth Factor Receptor-1 Regulates Postnatal Angiogenesis Through Inhibition of the Excessive Activation of Akt

Jun-ichiro Nishi,* Tohru Minamino,* Hideyuki Miyauchi, Aika Nojima, Kaoru Tateno, Sho Okada, Masayuki Orimo, Junji Moriya, Guo-Hua Fong, Kenji Sunagawa, Masabumi Shibuya, Issei Komuro

Abstract—Vascular endothelial growth factor (VEGF) binds both VEGF receptor-1 (VEGFR-1) and VEGF receptor-2 (VEGFR-2). Activation of VEGFR-2 is thought to play a major role in the regulation of endothelial function by VEGF. Recently, specific ligands for VEGFR-1 have been reported to have beneficial effects when used to treat ischemic diseases. However, the role of VEGFR-1 in angiogenesis is not fully understood. In this study, we showed that VEGFR-1 performs "fine tuning" of VEGF signaling to induce neovascularization. We examined the effects of retroviral vectors expressing a small interference RNA that targeted either the VEGFR-1 gene or the VEGFR-2 gene. Deletion of either VEGFR-1 or VEGFR-2 reduced the ability of endothelial cells to form capillaries. Deletion of VEGFR-1 markedly reduced endothelial cell proliferation and induced premature senescence of endothelial cells. In contrast, deletion of VEGFR-2 significantly impaired endothelial cell survival. When VEGFR-1 expression was blocked, VEGF constitutively activated Akt signals and thus induced endothelial cell senescence via a p53-dependent pathway. VEGFR-1$^{+/-}$ mice exhibited an increase of endothelial Akt activity and showed an impaired neovascularization in response to ischemia, and this impairment was ameliorated in VEGFR-1$^{+/-}$ Akt1$^{+/-}$ mice. These results suggest that VEGFR-1 plays a critical role in the maintenance of endothelial integrity by modulating the VEGF/Akt signaling pathway. (***Circ Res.* 2008;103:261-268.**)

Key Words: VEGF ■ Akt ■ senescence ■ p53

Angiogenesis involves the differentiation, proliferation, and migration of endothelial cells, leading to tubulogenesis and the formation of vessels.[1] One of the most important receptors for angiogenesis is the vascular endothelial growth factor (VEGF) receptor, which is a member of the receptor tyrosine kinase family.[2,3] VEGF receptor (VEGFR)-1 and VEGFR-2 are closely related receptor tyrosine kinases and have both common and specific ligands. VEGFR-1 has weaker kinase activity, whereas VEGFR-2 is a highly active kinase that stimulates a variety of signaling pathways and induces a broad range of biological responses. Despite its weak kinase activity, VEGFR-1 is essential for normal development and angiogenesis.[4] VEGFR-1 null mutant mice die in utero because of the overgrowth of endothelial cells and vascular disorganization.[5,6] In contrast, mice expressing the VEGFR-1 that lacks the tyrosine kinase domain develop a normal cardiovascular system,[7] suggesting that VEGFR-1 kinase activity might not be required for vascular development during embryogenesis and that VEGFR-1 may act as a decoy receptor. Consistent with this concept, selective activation of chimeric VEGFR-1 (in the absence of chimeric VEGFR-2)[8] or a VEGF mutant that binds to VEGFR-1 does not influence cell proliferation, migration, or survival in vitro.[9–11]

However, recent studies have demonstrated that the role of VEGFR-1 in postnatal angiogenesis is more complicated than was initially recognized. For example, treatment with placenta growth factor (PlGF), a specific ligand for VEGFR-1, was reported to promote angiogenesis in vitro[11,12] and in vivo.[13] Overexpression of PlGF also induced angiogenesis in tumors[14] and the skin.[15] It has been suggested that stimulation by PlGF induces the heterodimerization of VEGFR-1 with VEGFR-2, leading to transactivation of VEGFR-2 and the promotion of angiogenesis.[8,16,17] Another possible explanation for the positive effect of PlGF on angiogenesis is that it prevents VEGF from binding to VEGFR-1, thereby

Original received July 3, 2007; resubmission received February 18, 2008; revised resubmission received June 11, 2008; accepted June 16, 2008.

From the Department of Cardiovascular Science and Medicine (J.N., T.M., H.M., A.N., K.T., S.O., M.O., J.M., I.K.), Chiba University Graduate School of Medicine, Japan; PRESTO (T.M.), Japan Science and Technology Agency, Saitama, Japan; the Department of Physiology (G.-H.F.), University of Connecticut Health Center, Farmington; the Department of Cardiovascular Medicine (J.N., K.S.), Kyushu University Graduate School of Medical Sciences, Fukuoka, Japan; and the Department of Molecular Oncology (M.S.), Graduate School of Medicine and Dentistry, Tokyo Medical and Dental University, Japan.

*These authors contributed equally to this study.

Correspondence to Issei Komuro, MD, PhD, Department of Cardiovascular Science and Medicine, Chiba University Graduate School of Medicine, 1-8-1 Inohana, Chuo-ku, Chiba 260-8670, Japan. E-mail komuro-tky@umin.ac.jp

Circulation Research **is available at http://circres.ahajournals.org** **DOI: 10.1161/CIRCRESAHA.108.174128**

increasing the binding and activation of VEGFR-2. In other studies, PlGF was shown to protect against hyperoxic vascular damage in the retina without provoking retinal neovascularization.[18] These results suggest that VEGFR-1 can either positively or negatively regulate angiogenesis depending on the circumstances, but further studies are required to better understand the role of this receptor in postnatal angiogenesis.

In the present study, we examined the effects of VEGFR-1 deletion on angiogenesis by using the retroviral vector expressing a small interference RNA that targeted the VEGFR-1 gene. Deletion of VEGFR-1 markedly reduced endothelial cell proliferation and thus impaired angiogenesis. Likewise, VEGFR-1$^{+/-}$ mice exhibited an impaired neovascularization in response to ischemia. This impairment was restored by inhibiting the excessive activation of Akt by VEGF. These results suggest that VEGFR-1 plays a critical role in the maintenance of endothelial integrity by modulating the VEGF/Akt signaling pathway.

Materials and Methods

Short Hairpin Interference RNA Vectors

The mammalian retrovirus expression vector pSIREN-RetroQ (Clontech) was used to achieve the expression of short hairpin interference RNA (shRNA) in human endothelial cells.

Statistical Analysis

Data are shown as mean±SEM. Differences between groups were examined by Student *t* test or ANOVA followed by the Bonferroni procedure for comparison of means. Values of $P<0.05$ were considered statistically significant.

Results

Effect of VEGF Receptor Gene Silencing on Endothelial Cell Function

To elucidate the role of VEGFR-1 in angiogenesis, we constructed mammalian retroviral vectors expressing a short hairpin interference RNA that targeted either the VEGFR-1 gene (shVEGFR-1) or the VEGFR-2 gene (shVEGFR-2). Northern blot and Western blot analyses revealed that introduction of each construct into human umbilical vein endothelial cells caused effective and stable downregulation of the expression of the target molecule (Figure 1A and 1B, and supplemental Figure IA [available online at http://circres.ahajournals.org]). It is noted that either shVEGFR-1 or shVEGFR-2 did not affect VEGFR-2 or VEGFR-1 expression, respectively (Figure 1B, and supplemental Figure IA). We used two kinds of constructs for the following experiments and both of them achieved similar results. The nonsilencing control vector (shNega) was used as a control. After infected endothelial cells were purified by incubation with antibiotics, we performed the tube formation assay. Deletion of VEGFR-1 or VEGFR-2 significantly impaired tube formation compared with control cells (Figure 1C). We next examined the proliferative activity of infected cells. We seeded 2×10^5 infected cells into 100-mm dishes with VEGF-A on day 0 and counted cell number on day 3. Compared with shNega-infected control endothelial cells, both shVEGFR-1– and shVEGFR-2–infected cells showed significantly lower proliferation (Figure 1D). Deletion of VEGFR-1 caused more marked impairment of cell proliferation than deletion of VEGFR-2 (Figure 1D). This inhibitory effect of VEGFR-1 deletion was more evident when infected endothelial cells were subjected to long-term culture. Although VEGFR-2 deletion slightly reduced the lifespan of cells compared with that of control cells, VEGFR-1 deletion significantly shortened the lifespan of endothelial cells (Figure 1E). As a result, shVEGFR-1–infected cells underwent irreversible growth arrest earlier than shVEGFR-2-infected cells (Figure 1E). After growth arrest, the cells exhibited characteristics of senescence, becoming flatter and larger and showing an increase of senescence-associated β-galactosidase activity (Figure 1F). These findings suggest that VEGFR-1 deletion induces premature endothelial cell senescence. We next examined the effect of VEGFR-1 deletion on endothelial survival. We cultured infected cells in regular growth medium for 24 hours and subsequently cultured the cells under serum-free conditions with VEGF-A. After 24 hours, the number of viable cells was counted. As compared with the viability of control cells, deletion of VEGFR-2, but not VEGFR-1, markedly decreased cell viability (Figure 1G). Consistent with these findings, activation of caspase 3 was detected in cells with VEGFR-2 deletion, but not VEGFR-1 deletion (Figure 1H). These results suggest that VEGFR-1 is involved in the regulation of angiogenesis by regulating endothelial cell proliferation and senescence, whereas VEGFR-2 may be crucial for endothelial survival as well as cell proliferation.

VEGFR-1 Deletion Induces Endothelial Dysfunction by Activating Akt

To investigate the molecular mechanisms of premature senescence induced by VEGFR-1 deletion, we examined the transcriptional activity of p53 and its target gene p21. We transfected VEGFR-1–deleted endothelial cells with the luciferase reporter gene containing 13 copies of the p53-binding consensus sequence (pPG13-Luc). Deletion of VEGFR-1 significantly induced p53 transcriptional activity compared with that in shNega-infected cells, whereas VEGFR-2 deletion had no effect (Figure 2A). Likewise, p21 expression was significantly higher in VEGFR-1–deleted endothelial cells than in control cells or VEGFR-2–deleted cells (Figure 2B). However, expression of bax, another target molecule regulated by p53, was not altered in VEGFR-1–deleted endothelial cells compared with control cells (supplemental Figure IB). Ablation of p53 by the introduction of HPV16 E6 oncoprotein abolished the inhibitory effect of VEGFR-1 deletion on cell proliferation (Figure 2C). These results suggest that VEGFR-1 deletion induces endothelial cell senescence via a p53-dependent pathway.

We have previously demonstrated that Akt negatively regulates the endothelial cell lifespan by activating the p53/p21 pathway.[19] It has also been shown that Akt plays a central role in the regulation of angiogenesis by VEGF.[20] Thus, we examined the level of phosphorylated Akt in VEGFR-1-deleted endothelial cells. Western blot analysis

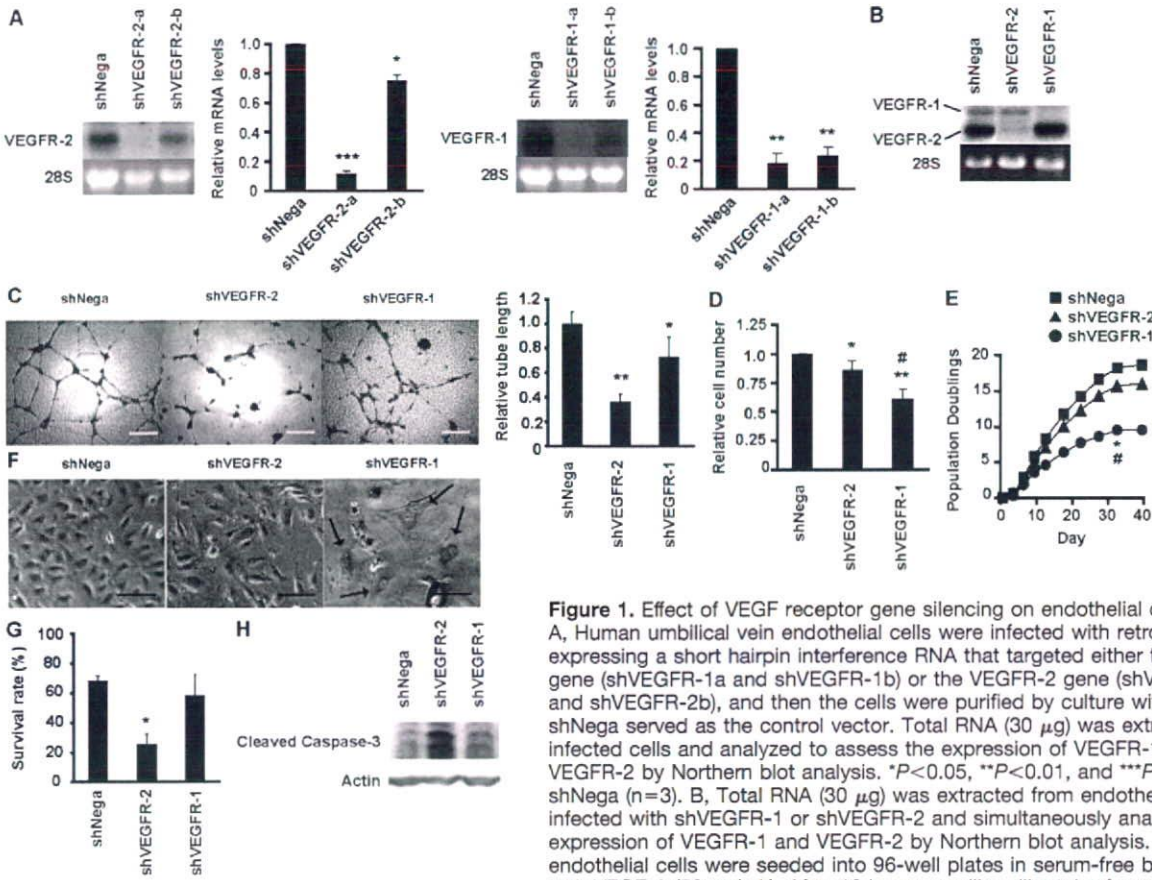

Figure 1. Effect of VEGF receptor gene silencing on endothelial cell function. A, Human umbilical vein endothelial cells were infected with retroviral vectors expressing a short hairpin interference RNA that targeted either the VEGFR-1 gene (shVEGFR-1a and shVEGFR-1b) or the VEGFR-2 gene (shVEGFR-2a and shVEGFR-2b), and then the cells were purified by culture with antibiotics. shNega served as the control vector. Total RNA (30 μg) was extracted from infected cells and analyzed to assess the expression of VEGFR-1 or VEGFR-2 by Northern blot analysis. *$P<0.05$, **$P<0.01$, and ***$P<0.001$ vs shNega (n=3). B, Total RNA (30 μg) was extracted from endothelial cells infected with shVEGFR-1 or shVEGFR-2 and simultaneously analyzed the expression of VEGFR-1 and VEGFR-2 by Northern blot analysis. C, Infected endothelial cells were seeded into 96-well plates in serum-free basic medium with VEGF-A (50 ng/mL). After 16 hours, capillary-like tube formation was estimated by using an angiogenesis image analyzer. *$P<0.01$, **$P<0.0001$ vs shNega (n=4 to 6). Scale bar: 300 μm. D, Infected endothelial cells were seeded at a density of 2×10^5 cells per 100-mm dish and cultured with VEGF-A (day 0). Then cell number was counted on day 3. *$P<0.001$, **$P<0.0001$ vs shNega, #$P<0.001$ vs shVEGFR-2 (n=13 to 14). E, Infected cell populations were passaged until cells underwent senescence, and the total number of population doublings was determined. *$P<0.01$ vs shNega, #$P<0.05$ vs shVEGFR-2 (n=4 to 6). F, Morphology and senescence-associated β-galactosidase staining (arrow) of endothelial cells infected with shNega, shVEGFR-1, or shVEGFR-2. Scale bar: 100 μm. G, Infected endothelial cells were seeded at the density of 1×10^5 cells per 60-mm dish and cultured for 24 hours in growth medium. After washing twice with PBS, the cells were cultured in serum-free DMEM with VEGF-A (10 ng/mL). After 24 hours of serum starvation, the number of viable cells and the total number of cells were counted by a hemocytometer. *$P<0.0001$ vs shNega (n=4 to 6). H, The lysates were extracted from cells, which are prepared as described in legend for G, and analyzed for cleaved caspase-3 expression by Western blotting.

showed that VEGFR-1 deletion led to a marked increase of the phosphorylated Akt level compared with that in control cells or cells with VEGFR-2 deletion, even under serum-free conditions (Figure 3A). VEGFR-1 deletion increased pAkt levels even in the absence of VEGF, presumably attributable to autocrine VEGF signaling (Figure 3B). Treatment with VEGF markedly increased pAkt levels within 5 to 15 minutes in VEGFR-1–deleted cells but not in VEGFR-2–deleted cells (Figure 3B). Treatment with a neutralizing anti-VEGF antibody reduced the phosphorylated Akt level in VEGFR-1-deleted cells (Figure 3C), suggesting that VEGFR-1 inhibits the activation of Akt by VEGF. To further investigate the relationship between constitutive Akt activation and endothelial cell dysfunction induced by VEGFR-1 deletion, we examined the effect of inhibition of Akt. We infected human endothelial cells with a retroviral vector encoding a dominant-negative form of Akt (DN-Akt)[19] or the empty vector encoding resistance to neomycin alone (Mock). Both cell populations were then infected with shNega or shVEGFR-1. We found that VEGFR-1 deletion markedly inhibited the proliferation of mock-infected endothelial cells (Figure 3D, Mock), whereas this inhibitory effect was significantly ameliorated in DN-Akt–infected cells (Figure 3D, DN-Akt). Consequently, VEGFR-1 deletion significantly impaired tube formation by mock-infected cells, but not DN-Akt-infected cells (Figure 3E). Likewise, inhibition of Akt activation prevented the induction of p21 expression by VEGFR-1 deletion (supplemental Figure II). These results suggest that VEGFR-1 deletion causes dysregulation of activation of the VEGFR-2/Akt signaling pathway by VEGF-A, and that constitutive activation of Akt is related to the impaired ability of VEGFR-1–deleted endothelial cells to proliferate and form capillary-like structures. VEGF-induced phosphorylation of eNOS was enhanced, but production of cGMP was significantly reducued by VEGFR-1 deletion, presumably because constitutive activation of Akt increases cellular reactive oxygen species[19] that inactivate this enzyme (supplemental Figure IC and ID).

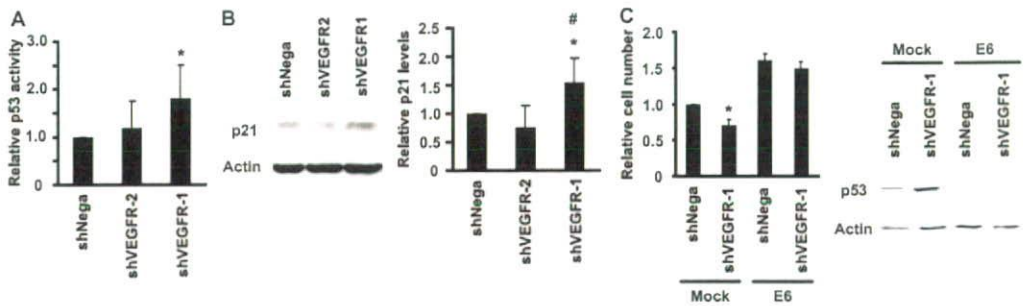

Figure 2. VEGFR-1 deletion induces activation of the p53/p21 signal pathway. A, A luciferase reporter gene plasmid (pPG13-Luc) containing the p53-binding sequence was transfected into endothelial cells infected with shNega, shVEGFR-1, or shVEGFR-2. Luciferase activity was measured at 48 hours after transfection in the presence of VEGF-A (10 ng/mL) as described in Methods. *$P<0.05$ vs shNega (n=5). B, Whole cell lysates (30 μg) were prepared from infected endothelial cells and p21 expression was assessed by Western blot analysis. *$P<0.05$ vs shNega, #$P<0.01$ vs shVEGFR-2 (n=4). C, Human endothelial cells were infected with pLNCX (Mock) or pLNCX E6 (E6). Infected cell populations were then transduced with shNega or shVEGFR-1. After purification, double-infected cells were seeded at a density of 2×10^5 cells per 100-mm dish in the presence of VEGF-A (day 0), and cell number was counted on day 3. *$P<0.05$ vs Mock/shNega (n=3). Western blot analysis revealed that introduction of E6 effectively ablated p53 expression (right panel).

Influence of VEGFR-1 Deletion on Neovascularization In Vivo

To examine the influence of VEGFR-1 deletion on neovascularization in vivo, we produced a hindlimb ischemia model in VEGFR-$1^{+/-}$ mice and assessed blood flow recovery and the capillary density of ischemic tissue. VEGFR-1 mRNA levels were significantly lower in VEGFR-$1^{+/-}$ mice than in wild-type mice (Figure 4A). Aortic expression of VEGFR-1 protein was decreased in VEGFR-$1^{+/-}$ mice compared with wild-type mice (Figure 4B). Consistent with the in vitro data, phospho-Akt levels were significantly higher in VEGFR-$1^{+/-}$ mice than in wild-type mice (Figure 4C and supplemental Figure III). There was no significant difference in plasma VEGF levels between the two groups (data not shown). Laser Doppler image analysis revealed that blood flow recovery was significantly impaired in VEGFR-$1^{+/-}$ mice compared with their wild-type littermates (Figure 4D). Likewise, VEGFR-$1^{+/-}$ mice exhibited significantly fewer CD31-positive cells in the ischemic tissues than their wild-type littermates (Figure 4E), suggesting that decreased expression of VEGFR-1 led to reduced neovascularization of ischemic tissue.

There are several reports indicating that VEGFR-1 kinase activity is required for VEGF-induced migration of hematopoietic cells including macrophages,[21–26] and it was reported that infiltration of macrophages plays a critical role in pathological angiogenesis during ischemia, inflammation, and tumor development.[27–29] Therefore, we examined the number of infiltrating macrophages in ischemic tissue, but we found no significant difference in the number of Mac3-

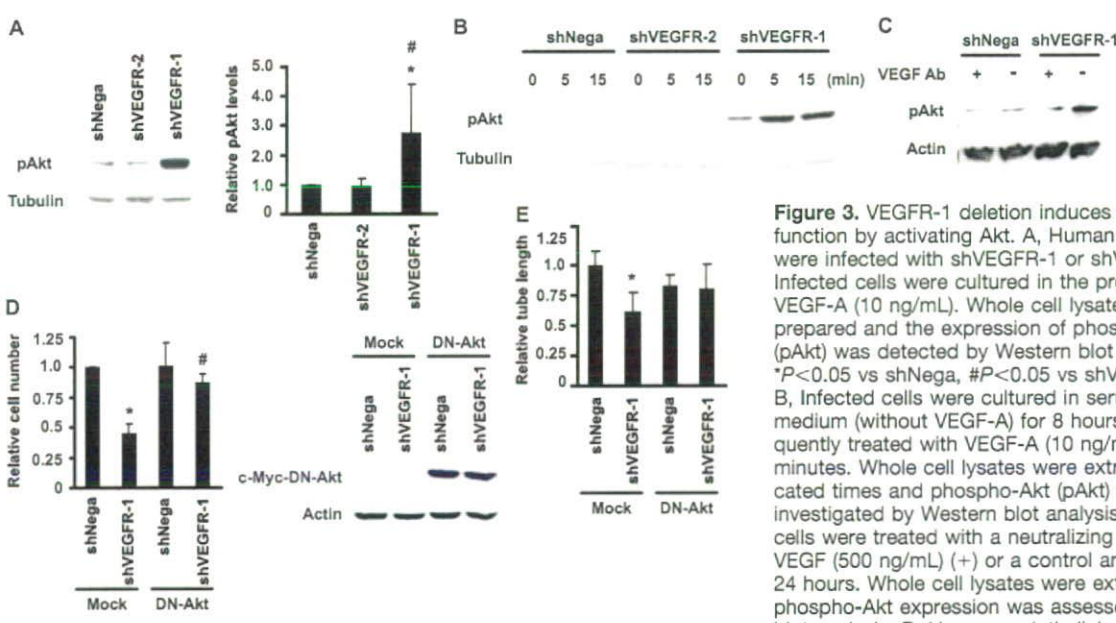

Figure 3. VEGFR-1 deletion induces endothelial dysfunction by activating Akt. A, Human endothelial cells were infected with shVEGFR-1 or shVEGFR-2. Infected cells were cultured in the presence of VEGF-A (10 ng/mL). Whole cell lysates (30 μg) were prepared and the expression of phosphorylated Akt (pAkt) was detected by Western blot analysis. *$P<0.05$ vs shNega, #$P<0.05$ vs shVEGFR-2 (n=5). B, Infected cells were cultured in serum-free basal medium (without VEGF-A) for 8 hours and subsequently treated with VEGF-A (10 ng/mL) for 5 to 15 minutes. Whole cell lysates were extracted at indicated times and phospho-Akt (pAkt) expression was investigated by Western blot analysis. C, Infected cells were treated with a neutralizing antibody for VEGF (500 ng/mL) (+) or a control antibody (−) for 24 hours. Whole cell lysates were extracted and phospho-Akt expression was assessed by Western blot analysis. D, Human endothelial cells were infected with pLNCX (Mock) or pLNCX DN-Akt (DN-Akt). Infected cell populations were then transduced with shNega or shVEGFR-1 and were subjected to the proliferation assay as described in legend for Figure 2C. *$P<0.005$ vs Mock/shNega, #$P<0.005$ vs Mock/shVEGFR-1 (n=6 to 8). Expression of c-Myc-tagged DN-Akt was confirmed by Western blot analysis (right panel). E, Double-infected endothelial cells (prepared as in Figure 3C) were subjected to the tube-forming assay. *$P<0.05$ vs Mock/shNega (n=3).